

Disentangling Geometric Deformation Spaces in Generative Latent Shape Models

Tristan Aumentado-Armstrong^{1,2,3} · Stavros Tsogkas^{1,2} · Sven Dickinson^{1,2,3} · Allan Jepson^{1,2}

Abstract A complete representation of 3D objects requires characterizing the space of deformations in an interpretable manner, from articulations of a single instance to changes in shape across categories. In this work, we improve on a prior generative model of geometric disentanglement for 3D shapes, wherein the space of object geometry is factorized into rigid orientation, non-rigid pose, and intrinsic shape. The resulting model can be trained from raw 3D shapes, without correspondences, labels, or even rigid alignment, using a combination of classical spectral geometry and probabilistic disentanglement of a structured latent representation space. Our improvements include more sophisticated handling of rotational invariance and the use of a diffeomorphic flow network to bridge latent and spectral space. The geometric structuring of the latent space imparts an interpretable characterization of the deformation

Tristan Aumentado-Armstrong^{1,2,3}
E-mail: tristan.aumentado@mail.utoronto.ca

Stavros Tsogkas^{1,2}
E-mail: tsogkas@cs.toronto.edu

Sven Dickinson^{1,2,3}
E-mail: sven@cs.toronto.edu

Allan Jepson^{1,2}
E-mail: jepson@cs.toronto.edu

¹ University of Toronto

² Samsung Toronto AI Research Center

³ Vector Institute for Artificial Intelligence

Disclaimer: Tristan Aumentado-Armstrong and Stavros Tsogkas contributed to this article in their personal capacity as PhD student and Adjunct Professor at the University of Toronto, respectively. Sven Dickinson and Allan Jepson contributed to this article in their personal capacity as Professors at the University of Toronto. The views expressed (or the conclusions reached) by the authors are their own and do not necessarily represent the views of Samsung Research America, Inc.

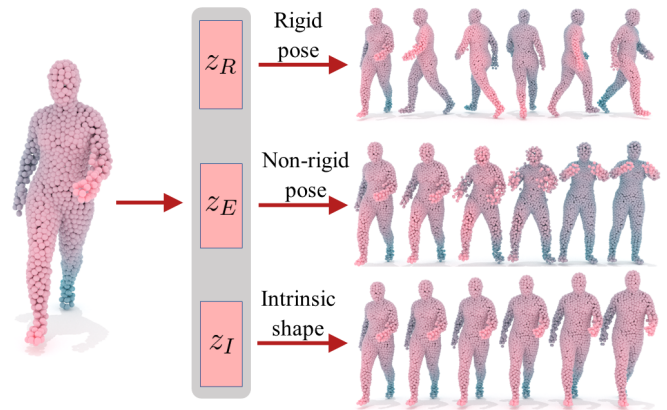


Fig. 1 Depiction of overall framework goal. We factorize the latent deformation space of a given 3D object into rigid pose z_R , extrinsic non-rigid pose z_E , and intrinsic shape z_I , without supervision.

space of an object. Furthermore, it enables tasks like pose transfer and pose-aware retrieval without requiring supervision. We evaluate our model on its generative modelling, representation learning, and disentanglement performance, showing improved rotation invariance and intrinsic-extrinsic factorization quality over the prior model.

Keywords 3D Shape · Generative Models · Disentanglement · Articulation · Deformation · Representation Learning

1 Introduction

A major goal of representation learning is to discover and separate the underlying explanatory factors that give rise to some set of data (Bengio et al., 2013). For

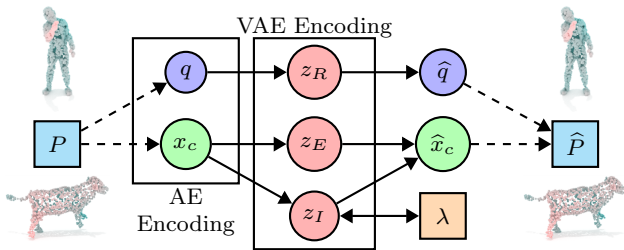


Fig. 2 A schematic overview of the combined two-level architecture used as the generative model. A point cloud P is first encoded into (q, x_c) by a *deterministic* AE, where q is the quaternion representing the rotation (rigid pose) of the shape, and x_c the compressed representation of the input P , in its *canonical* orientation. (q, x_c) is then further compressed into a latent representation $z = (z_R, z_E, z_I)$ of a VAE. The hierarchical latent variable z has disentangled subgroups in red (representing rotation, extrinsics, and intrinsics, respectively). The intrinsic latent subgroup z_I is used to contain the information in the LBO spectrum λ using an invertible mapping. Both the extrinsic z_E and intrinsic z_I are utilized to compute the shape \hat{x}_c in the AE’s latent space. The latent rotation z_R is used to predict the quaternion \hat{q} . Finally, the decoded representation (\hat{q}, \hat{x}_c) is used to reconstruct the original point cloud \hat{P} . The deterministic AE mappings are shown as dashed lines; VAE mappings are represented by solid lines.

many objects, such as 3D shapes of biological entities, structuring their representation within a learned model means understanding the different modes of their deformation spaces. For instance, rotating a chair does not affect its category, nor does articulated deformation of a cat alter its identity. In general, different geometric deformations may be semantically distinct, e.g., shape style (Marin et al., 2020), intrinsic versus extrinsic alterations (Corman et al., 2017), or geometric texture details (Berkiten et al., 2017). In other words, for many objects, we can naturally factorize the associated deformation space, based on geometric characteristics.

Such a disentanglement can provide a useful structuring of the 3D shape representation. For example, in a vision context, one could constrain inference of a 3D model from a motion sequence to change in pose, but not intrinsic shape. Or, in the context of graphics, separating shape and pose allows for tasks such as deformation transfer or shape interpolation.

In this work, we consider a purely geometric decomposition of object deformations, separating the space into rigid orientation, non-rigid pose, and shape. Our method is based on methods from spectral geometry, utilizing the isometry invariance of the Laplace-Beltrami operator spectrum (LBOS). The LBOS characterizes the intrinsic geometry of the shape; in contrast, we refer to the space of non-rigid isometric deformations of the shape as its extrinsic geometry, in a manner similar to (Corman et al., 2017). This decomposition is performed in the latent space of a generative model, using

information-theoretic methods for disentangling random variables, resulting in three latent vectors for rigid orientation, pose, and shape. We apply our model to several tasks requiring this factorized structure, including pose-aware retrieval and pose-versus-shape interpolation (for which pose transfer is a special case). See Fig. 2 for an overview of our approach.

We focus on minimizing the supervision required for our model, eschewing requirements for identical meshing, correspondence, or labels. Thus, our method is orthogonal to advances in neural architectures, as it can be applied to any encoder or decoder model. For the same reason, it is also agnostic to the 3D modality (e.g., meshes, voxels, or implicit fields), but we choose to focus on point clouds, as they are a common data type in computer vision.

Our method builds on a prior model (Aumentado-Armstrong et al., 2019), the geometrically disentangled VAE (GDVAE), with two major algorithmic improvements: (1) we enhance the ability of the network to factorize rotation, investigating two representation learning approaches that allow the model to correctly discern a canonical rigid orientation, and (2) we replace a simple spectrum regressor with a diffeomorphic flow network. This allows us to define a better training procedure, in which we use a shape-from-spectrum starting point, instead of the initial input shape, thus ensuring that the latent intrinsics cannot access extrinsics. These two improvements result in superior disentanglement quality, compared to the prior GDVAE model.

2 Background

2.1 Rotation Invariant Shape Representation

Invariance to rotation is generally a desirable property of shape representations, since many tasks (such as categorization or retrieval) tend to consider orientation a nuisance variable. Hence, there is a significant body of work on how to learn such rigid invariance.

Classical research includes many types of geometric features, directly computed from input shapes, that are rotation invariant (e.g., Guo et al. (2014)), such as structural indexing (Stein et al., 1992), signature of histogram orientations (Tombari et al., 2010), spin images (Johnson and Hebert, 1999), and point signatures (Chua and Jarvis, 1997). More recently, SRINet (Sun et al., 2019), ClusterNet (Chen et al., 2019a), and RINet (Zhang et al., 2019) design rotation invariant hand-crafted features that can be extracted from point clouds (PCs), for use in learning algorithms.

Separately, rotation *equivariance* has been achieved in voxel shapes using group convolutions (Worrall and

Brostow, 2018) and spherical correlations (Cohen et al., 2018), which can be utilized to obtain invariance. PRIN (You et al., 2018) computes rotation invariant features for point clouds, but requires the application of convolutions on spherical voxel grids. SPHNet (Poulenard et al., 2019) attains rotation invariance without voxelization, by extending feature signals defined on a shape into \mathbb{R}^3 , and then using a specific non-linear transform of the signal, convolved with a spherical harmonic kernel.

Other works focus on changing the input and/or utilizing other representation learning techniques, which are more closely related to our work. The PCA-RI model (Xiao et al., 2020) achieves rotation invariance by transforming each shape into an intrinsic reference frame, defined by its principal components, handling frame ambiguity (due to eigenvector signs) by duplicating the input. Info3D (Sanghi, 2020) uses techniques from unsupervised contrastive learning to encourage rotation invariance in the representation, including the ability to handle unaligned data. Li et al. (2019) attain equivariance by rotating each input point cloud by a discrete rotation group. Similar to this, a rotation invariant encoder can be defined by feeding in randomly rotated copies of the input (Sanghi and Danielyan, 2019). We build on this latter approach to define one version of our 3D autoencoder (AE). For our other approach, we utilize Feature Transform Layers (FTLs) (Worrall et al., 2017), which allow us to make latent space rotations equivalent to 3D data space rotations. In both cases, rather than remove rigid transforms from the embedding, we attempt to factorize such transforms out, as part of the deformation space of the object.

More specifically, we consider two general approaches to learning rotation invariant representations, building on related work as noted above. Both methods are modality agnostic (e.g., not requiring spherical voxelization), architecture independent (e.g., not necessitating particular types of convolution), able to avoid information loss in feature extraction, and do not increase the cost of a forward pass (e.g., no duplication of inputs). In this sense, our method is largely orthogonal to architectural improvements for PC processing, as well as the aforementioned approaches to rotation invariance. Indeed, they can be readily applied to other 3D shape modalities. This is because our approaches modify only the latent representation and loss calculation procedure, allowing the us use arbitrary features as input, including rotation invariant ones. Nevertheless, we show that, despite obtaining features from a simple PointNet (Qi et al., 2017), we can still attain rotation invariance without architectural alterations. Finally, the utility of much of the related work above for generative modelling and/or autoencoding is unclear; hence, we choose to use simpler

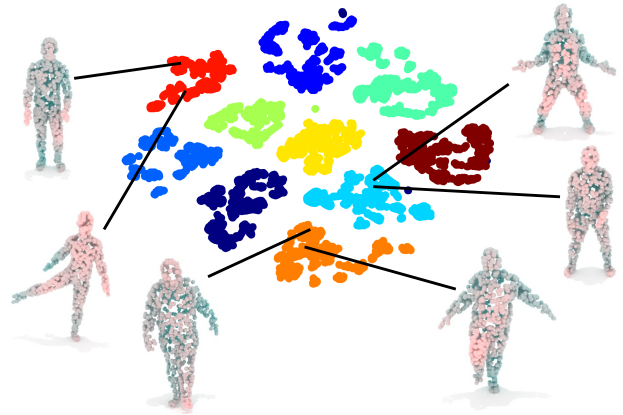


Fig. 3 Pose versus shape factorization via LBOS. A t-sne (van der Maaten and Hinton, 2008) plot of LBOSs from the Dyna dataset (Pons-Moll et al., 2015), with illustrative accompanying point cloud representations for several spectra. Different body shapes are mapped close together, regardless of articulated pose.

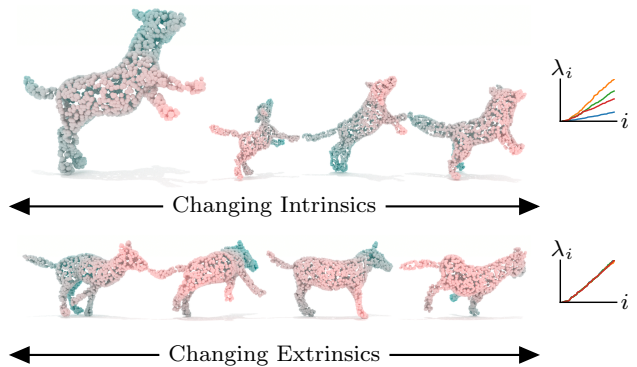


Fig. 4 Visual explanation of the use of spectral geometry in characterizing intrinsic versus extrinsic shape. We display two rows of animals, showing different *intrinsic*s (first row) and *extrinsic*s (second row), across the columns per inset. The plots show the LBOS λ across shapes (indices i range from 1 to 50); notice the lack of variability as extrinsics change.

architectures already known to work for these purposes (Achlioptas et al., 2017; Aumentado-Armstrong et al., 2019).

2.2 Shape Analysis via Spectral Geometry

Any 3D surface can be viewed as a 2D Riemannian manifold (\mathcal{M}, g) , with metric tensor g , which allows the application of differential geometry to shape analysis in computer graphics and vision. One major technique in this area is the use of *spectral geometry*, which is mainly concerned with the Laplace-Beltrami Operator (LBO), Δ_g , and its associated spectrum (i.e., the eigenvalues λ of $-\Delta_g \phi_i = \lambda_i \phi_i$) for shape processing (Patané, 2016). Use of the spectrum generalizes classical Fourier analysis on Euclidean domains to manifolds, transfer-

ring concepts from signal processing to transforms of non-Euclidean geometry itself (Taubin, 1995). The LBO spectrum (LBOS) characterizes the intrinsic properties of a manifold (Lévy, 2006; Rustamov, 2007; Vallet and Lévy, 2008), sufficiently matching human intuition on the meaning of “shape”, to the extent it is considered as its “DNA” (Reuter et al., 2006). Mathematically, *intrinsic* properties of a shape are those that depend only on its metric tensor, independent of its embedding (Corman et al., 2017); this includes, for example, geodesic distances and the LBOS. Among the most useful advantages of intrinsic shape properties is *isometry invariance*, meaning intrinsics do not change in response to alterations that do not affect the metric. This includes rigid transforms, as well as non-rigid deformations, such as biological articulations (approximately). Algorithms relying on shape intrinsics are therefore able to ignore such deformations (e.g., recognize a person regardless of articulated pose). We show some examples of the intrinsic-extrinsic geometric decomposition provided by the LBOS in Figures 3 and 4.

Intrinsic spectral geometry processing has thus yielded numerous useful techniques for vision and graphics, often due to its isometry invariance. This includes semi-localized, articulation invariant feature extraction, such as the heat (Sun et al., 2009; Gebal et al., 2009) and wave (Aubry et al., 2011) kernel signatures, later extended to learned generalizations (Boscaini et al., 2015b). Similar techniques can be applied to a variety of downstream tasks for 3D shapes as well, including correspondence (Rodolà et al., 2017; Ovsjanikov et al., 2012), retrieval (Bronstein et al., 2011), segmentation (Reuter, 2010), analogies (Boscaini et al., 2015a), classification (Mansouri and Hamza, 2017), and manipulation (Vallet and Lévy, 2008). Beyond the standard LBOS, more recent research has also explored localized manifold harmonics (Neumann et al., 2014; Melzi et al., 2018), modifications of the LBO (Choukroun et al., 2018; Andreux et al., 2014), and *extrinsic* spectral geometry (Liu et al., 2017; Ye et al., 2018; Wang et al., 2017).

In this work, we focus on utilizing the classical LBOS as a purely intrinsic characterization of the shape. By exploiting the approximate articulation invariance conferred by its isometry invariance, we gain access to a signal that can separate intrinsic shape from articulated pose, without supervision beyond the geometry itself. While the LBO has been used to perform disentangled shape manipulations in the context of computer graphics, such as isometric shape interpolation (Baek et al., 2015) and spectral pose transfer (Yin et al., 2015), we show how to do such manipulations within a generative model, as a byproduct of the learned representation.

2.3 Learning Shape-Pose Disentanglement

A common task that has been tackled in the context of computer graphics is *pose transfer*. Utilizing a small set of correspondences, an optimization-based approach can be applied to perform deformation transfer (Sumner and Popović, 2004). Later work utilized the LBO eigenbases to perform pose transfer (Kovnatsky et al., 2013; Yin et al., 2015), via exchanging low-frequency coefficients of the manifold harmonics. In our work, we use the LBOS instead, which avoids issues of basis computation and spectral compatibility (Kovnatsky et al., 2013). Basset et al. (2020) consider transferring shape instead of pose; due to our symmetric formulation, our approach is also capable of this. We refer to Roberts et al. (2020) for a survey of related work.

Recently, several works have attacked pose transfer from a machine learning point of view. Gao et al. (2018) present a method for mesh deformation transfer using a cycle consistent GAN and a visual similarity metric, but require retraining new models for each source and target set. Levinson et al. (2019) utilize a mesh VAE, which relies on data having identical meshing, to separate pose and shape via batching with identical pose and shape labels. LIMP (Cosmo et al., 2020) disentangles intrinsic and extrinsic deformations in a generative model, utilizing a differentiable geodesic distance regularizer; identical meshing or labels are not required, though correspondence is. Zhou et al. (2020) devise a method for separating intrinsics and extrinsics using corresponding meshes known only to have the same shape but different pose, and applying a powerful as-rigid-as-possible geometric prior. Finally, Marin et al. (2020) consider learning from the LBOS as well, examining its use in the context of neural networks for several tasks, including spectrum estimation from point clouds and shape style transfer; however, they do not focus on deformation space factorization or generative representation learning.

In our work, we focus on learning a generative representation that factorizes the latent deformation space into intrinsic shape and extrinsic pose, without supervision. We do not require labels (e.g., identity, pose, or shape), identical meshing, correspondence, or even rigid alignment – only the raw geometry, which we use to compute the LBOS. Rather than targeting pose transfer specifically, in our model, the ability to transfer articulation arises naturally from the learned representation. In particular, we build on the GDVAE model (Aumentado-Armstrong et al., 2019), which disentangles shape and pose into two continuous and independent latent factors. Our method, which we refer to as the GDVAE++ model, includes adding a bijective mapping from an LBO spec-

trum to the space of latent intrinsics, and defining a new training scheme based on this function. We show that the resulting model is significantly improved in terms of disentanglement.

3 Autoencoder Model

Our model consists of two components: an autoencoder (AE) on the 3D shape data and a variational autoencoder (VAE) defined on the latent space of the AE. We show an overview of the complete framework in Fig. 2.

In this work, the AE is used to map a 3D point cloud (PC) to a latent vector, and then decode it back to a reconstruction of the original input. In contrast to the AE used in the prior GDVAE model (Aumentado-Armstrong et al., 2019), we specifically consider the rotational invariance properties of the AE architecture.

Notation. We assume our input is a PC $P \in \mathbb{R}^{N_p \times 3}$, which we want to reconstruct as $\hat{P} \in \mathbb{R}^{N_p \times 3}$. To do so, we encode P into a rigid rotation, represented as a quaternion $q \in \mathbb{R}^4$, and canonically oriented non-rigid latent shape, $x_c \in \mathbb{R}^n$, using learned mappings E_r and E_x . We can also obtain a canonical PC, $P_c = D(x_c) \in \mathbb{R}^{N_p \times 3}$, via a decoder D . The details for obtaining this rigid versus non-rigid factorization are given below.

3.1 Autoencoder Architecture

We consider two possible AE architectures on PCs. Both models attempt to regress a rotation matrix and a rotation invariant latent shape representation from an input. The first type, which we denote “standard” (STD), uses a straightforward reconstruction loss, but also includes a random rotation before attempting to encode the shape, inspired by prior work (Sanghi and Danielyan, 2019; Li et al., 2019). The second type relies on feature transform layers (FTLs) (Worrall et al., 2017) to learn a latent vector space that transforms covariantly with the 3D data space under rotation, thus allowing the model to learn how to “derotate” to a canonical representation (denoted “FTL-based”).

Implementation-wise, we use PointNet (Qi et al., 2017) to encode an input point cloud, P (which allows us to handle dynamic PC sizes), and fully connected layers (with batch normalization and ReLU) for all other learned mappings, unless otherwise specified. See Appendix Sec. D.1 for details.

3.1.1 Standard Architecture

Let P be an input PC, that has potentially undergone an arbitrary rotation. We learn two mappings as our

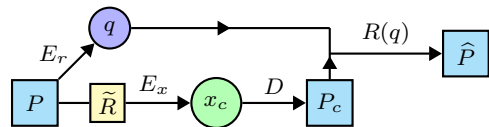


Fig. 5 STD AE architecture. Our standard AE encodes an input PC P into a rigid pose component (quaternion q) and canonically oriented shape embedding x_c . Before passing P to the shape encoder E_x , a random rotation \tilde{R} is sampled and applied. The decoder D then generates the canonical PC P_c , which is rotated by $R(q)$ into the final reconstruction \hat{P} .

encoder, E_r and E_x , which map P to a quaternion $q = E_r(P)$ and a latent shape embedding $x_c = E_x(P)$. Our decoder D generates a canonically oriented PC $P_c = D(x_c)$, which can be rotated to match the input via $\hat{P} = P_c R(q)$, where $R(q)$ is the parameter-less conversion from quaternion to rotation matrix. Inspired by (Sanghi and Danielyan, 2019; Li et al., 2019), we insert an additional layer before E_x that randomly rotates P (i.e., $x_c = E_x(P\tilde{R})$, \tilde{R} being a random sample), to further encourage learning rotation invariant features. We only do this for the standard architecture, shown in Fig. 5.

3.1.2 FTL-based Architecture

We also consider a slightly more complex architecture with a latent space designed for interpretability under rotation transformations, using a Feature Transform Layer (FTL) (Worrall et al., 2017). Our design is inspired by prior work (Remelli et al., 2020) that extracts *canonical representations* in the context of 3D human pose using FTLs. Nevertheless, the architecture components of the FTL-AE are nearly the same as those of the STD-AE.

Rotational Feature Transform Layers. The main idea behind FTLs is to view a latent vector $x \in \mathbb{R}^n$ as an ordered set of subvectors $U[x] = (u[x]_1, \dots, u[x]_{N_s}) \in \mathbb{R}^{N_s \times 3}$, where $N_s = n/3$ and $u[x]_i \in \mathbb{R}^3$, by simply unfolding it into a matrix. Consider rotating a point cloud $P \in \mathbb{R}^{N_p \times 3}$ by a 3D rotation operation $R \in \mathbb{R}^{3 \times 3}$, to get a new shape PR . By unfolding, one can analogously perform this rigid transformation on a “latent point cloud”, as $U[x]R$. Ideally, applying R to P or $U[x]$ has the *same effect* (i.e., rotates the underlying shape in the same way), resulting in an interpretable latent space, with respect to rotation. We define the rotational feature transform layer $F(R, x) = U^{-1}[U[x]R]$ as a latent rotation R of the subvectors of x , where the inverse U^{-1} “refolds” the ordered set of subvectors into a single vector-valued latent variable again (as opposed to the “unfolding” operator U). We will use the FTL mapping F to enforce a rotation equivariant structure onto the latent space, thus allowing us to “derotate” the shape

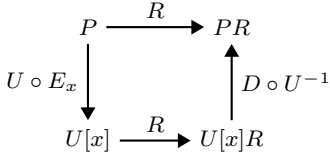


Fig. 6 Desired commutativity structure of FTL-based architecture. Ideally, latent rotations should have the same effect as in the data space.

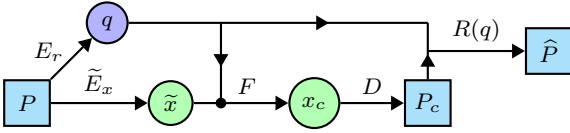


Fig. 7 FTL-based AE architecture. An input PC, P , is encoded into a quaternion q and a *pose-aware* embedding \tilde{x} , representing the rotated (rather than the canonical) shape. The rotational FTL F is then used to de-rotate \tilde{x} to obtain the *canonically* oriented shape $x_c = E_x(P) = F(R(q), \tilde{x})$. Finally, a reconstruction of the input, \hat{P} , is produced by rotating the decoded canonical PC $P_c = D(x_c)$ using the predicted rigid pose $R(q)$.

embedding to some canonical rigid pose. We depict the desired duality over rotations in Fig. 6.

Architectural Details. Utilizing similar notation to Sec. 3.1.1, we first encode $q = E_r(P)$, as before, and convert it to a predicted rotation $\hat{R} = R(q)$. We then compute a *non-canonical* latent shape $\tilde{x} = \tilde{E}_x(P)$, which encodes the *rotated* shape P . We then use the FTL to obtain the canonical latent shape via $x_c = F(\hat{R}, \tilde{x})$, which can be decoded via $P_c = D(x_c)$ with shared parameters. As before, we obtain the final reconstruction via $\hat{P} = P_c \hat{R}$. For notational consistency, we write $E_x(P) = x_c = F(\hat{R}, \tilde{E}_x(P))$. See Fig. 7 for a visual depiction.

This FTL-based architecture provides greater interpretability in terms of the effect of a rigid transform on the representation; rather than trying to remove the dependence on rotation, we attempt to explicitly characterize it. Rotations in the 3D *data* space should thus have an identical effect on the resulting *latent* space representation (and vice versa).

3.2 Autoencoder Loss Objective

The overall loss function for the AE can be written

$$\mathcal{L}_{\text{AE}} = \mathcal{L}_c + \mathcal{L}_R + \mathcal{L}_P + \mathcal{L}_x, \quad (1)$$

where the terms control representational consistency \mathcal{L}_c , rotation prediction \mathcal{L}_R , reconstruction \mathcal{L}_P and regularization \mathcal{L}_x . These terms will be different depending on whether one uses the STD-AE (Sec. 3.1.1) or FTL-AE (Sec. 3.1.2).

3.2.1 Standard Loss Objective

Reconstruction Loss. The reconstruction loss term for the STD architecture is $\mathcal{L}_P = \gamma_P D_P(P, P_c)$, where D_P includes a Chamfer distance and an approximate Hausdorff loss, similar to prior work (Aumentado-Armstrong et al., 2019; Chen et al., 2019b):

$$D_P(P_1, P_2) = \alpha_C d_C(P_1, P_2) + \alpha_H d_H(P_1, P_2), \quad (2)$$

in which the squared L_2 distance is used between matched points.

Cross-Rotational Consistency Loss is a simple loss designed to promote consistency of the latent representation across rotations of the input, i.e., encourage rotation invariance. First, we split each batch into n_R copies of the same PCs; we then apply a different random rotation to each copy. Letting $x_{c,i}$ be the embedding of P after having undergone the i th rotation, the loss is then

$$\mathcal{L}_c = \frac{\gamma_c}{M_c} \sum_{i=1}^{n_R} \sum_{j>i} \|x_{c,i} - x_{c,j}\|_2^2, \quad (3)$$

where M_c is the number of pairwise distances. Note that, unlike combining features across rotated copies (Xiao et al., 2020; Li et al., 2019), this approach does not increase the computational cost of a forward pass for a single input.

Rotation Loss depends on whether we assume the data is rigidly aligned or unaligned, i.e., whether we have rotational supervision or not. In the supervised case, where the canonical rigid pose is shared across data examples, we simply predict the real rotation for every example: $\mathcal{L}_R = \gamma_R d_R(R, \hat{R})$, where

$$d_R(R_k, R_\ell) = \frac{1}{\pi} \arccos \left(\frac{\text{tr}(R_k R_\ell^T) - 1}{2} \right) \quad (4)$$

is the geodesic distance on $SO(3)$ (Huynh, 2009).

In the *unsupervised* case, we enforce a consistency loss across rotational predictions, which does not rely on a ground truth P being canonical across multiple shapes. Instead, it only asks that the predicted rotations of an object have the same *relative* difference as the original rotations of the input (which should be true regardless of whether P was originally canonically oriented). Consider rotations of a PC, $P_i = P_0 R_0 R_i$, where our data follows $P = P_0 R_0$, in which P_0 (the ground truth PC in canonical orientation) and R_0 (the rotation of the ground truth datum) are both unknown. Our predictions are $\hat{P}_i = P_c \hat{R}_i$, so for any two rotations of a single observed PC (e.g., P_i and P_j), we want $\hat{R}_i \approx R_0 R_i$

and $\widehat{R}_j \approx R_0 R_j$, meaning we want to predict R_k relative to R_0 . Combining these equations means we want $R_i^T \widehat{R}_i \approx R_j^T \widehat{R}_j$ for each such pair. Formally, we write this constraint as

$$\mathcal{L}_R = \frac{\gamma_r}{M_c} \sum_{i=1}^{n_R} \sum_{j>i} d_R(R_i^T \widehat{R}_i, R_j^T \widehat{R}_j), \quad (5)$$

where R_k and \widehat{R}_k are the true and predicted rotations for the k th copy in the duplicated batch, respectively. As noted above, in the unsupervised case, we do not necessarily wish to regress R_i as \widehat{R}_i , because the initial (derotated) input P is not assumed to be in the canonical orientation of P_c .

Regularization Loss. The primary purpose of the AE is to provide a space with reduced complexity and dimensionality, for taining the generative VAE model. Following work on learning probabilistic samplers with latent-space generative autoencoders (Ghosh et al., 2019), we apply a small weight decay and latent radius loss: $\mathcal{L}_x = \gamma_w L_2(\Theta) + \gamma_d \|x_c\|_2^2$, where $L_2(\Theta)$ is an L_2 weight decay on the network parameters Θ .

3.2.2 FTL-based Loss Objective

Similar to the network functions, the FTL-AE objective terms, as well as the training regime, are largely reused from the STD-AE. The only major difference is that we compute reconstruction losses for both the instance representation, \tilde{x} , and the canonical representation, x_c :

$$\mathcal{L}_P = \gamma_{\tilde{P}} D_P(P_r, \tilde{P}) + \gamma_P D_P(P, P_c). \quad (6)$$

Here, the decoder output $\tilde{P} = D(\tilde{x})$ is encouraged to be similar to the rotated input P_r .

We note that the penalty \mathcal{L}_c , enforcing consistency of the canonical latent shape vectors $x_{c,j}$ in the FTL architecture, ties the non-canonical embeddings, \tilde{x}_j , through an FTL operation (across rotated inputs), as follows:

$$\|x_{c,i} - x_{c,j}\|_2^2 = \|(U[\tilde{x}_i]R_i - U[\tilde{x}_j]R_j)R_i^T\|_F^2 \quad (7)$$

$$= \|U[\tilde{x}_i] - U[\tilde{x}_j]R_j R_i^T\|_F^2, \quad (8)$$

where we have used $U[x_{c,k}] = U[\tilde{x}_k]R_k$, and the orthogonality of R_k implies $\|R_k v\|_2^2 = \|v\|_2^2$ for any $v \in \mathbb{R}^3$.

4 Latent Variational Autoencoder Model

4.1 Overview

Our goal is to define a disentangled generative model of 3D shapes, using a VAE. The model should be capable of encoding for representation inference, decoding

random noise for novel sample generation, and allowing factorized latent control of intrinsic shape and extrinsic non-rigid pose. The latter decomposition is made possible by use of the LBO spectrum, which allows us to separate non-rigid deformations into intrinsic shape and articulated pose (see Sec. 2.2).

Following Ghosh et al. (2019); Achlioptas et al. (2017), we use the AE latent space to define our generative model and disentangled representation learning. This allows us to train with much larger batch sizes (useful for information-theoretic objectives based on estimating marginal distribution properties from samples), and generally obtain better computational efficiency. See Fig. 2 for a pictographic overview.

Compared to our prior GDVAE model (Aumentado-Armstrong et al., 2019), we replace a simple predictor of the LBOS from the latent intrinsic shape with a diffeomorphic mapping between the two quantities. This allows us to use the spectrum directly in training (see Sec. 4.4) and increase the dimensionality of the latent intrinsics, improving representation performance.

4.2 Model Architecture

4.2.1 Hierarchically factorized VAE

The core of our VAE model is the Hierarchically factorized VAE (HFVAE) model (Esmaili et al., 2018), which permits penalization of mutual information between sets of vector-valued random variables. This allows us to enforce the latent intrinsics to be separate from the latent extrinsics, specifically.

Let (q, x_c) be an encoded input from the AE. We define $z_R \sim \mathcal{N}(\mu_R(q), \Sigma_R(q))$, $z_E \sim \mathcal{N}(\mu_E(x_c), \Sigma_E(x_c))$, and $z_I \sim \mathcal{N}(\mu_I(x_c), \Sigma_I(x_c))$ to be the latent encodings of the rotation, extrinsic shape, and intrinsic shape, respectively, sampled from their variational latent posteriors. Our decoder is deterministic: $\widehat{q} = D_q(z_R)$ and $\widehat{x}_c = D_x(z_E, z_I)$. All three variables use isotropic Gaussians as latent priors. See Appendix Sec. D.2 for further details.

4.2.2 Normalizing Flow for Spectrum Encoding

In order to encourage z_I to hold only shape intrinsics, we utilize the LBOS. In particular, we define an invertible mapping between λ and μ_I . Let $\tilde{\mu}_I = \widehat{f}_\lambda(\lambda)$ be the latent encoding of a real spectrum, λ , and $\widehat{\lambda} = g_\lambda(\mu_I)$ be the predicted spectrum, with $g_\lambda = \widehat{f}_\lambda^{-1}$. We implement \widehat{f}_λ as a normalizing flow network (Papamakarios et al., 2019; Kobayev et al., 2020), defining a diffeomorphism between z_I -space and the space of spectra.

Using a flow mapping ensures that $f_\lambda(\lambda)$ can hold complete information about λ . Unlike [Aumentado-Armstrong et al. \(2019\)](#), this approach also allows “shape-from-spectrum” computation ([Marin et al., 2020](#)), though we leave this to future work. Finally, it has the added benefit of being specifically designed for likelihood-based generative modelling, hence its training procedure synergizes well with the HFVAE.

4.3 VAE Loss Function

The VAE model is trained with the following objective:

$$\mathcal{L}_{\text{VAE}} = \mathcal{L}_{\text{HF}} + \mathcal{L}_\lambda + \mathcal{L}_F + \mathcal{L}_D, \quad (9)$$

where \mathcal{L}_{HF} is the hierarchically factorized VAE loss ([Esmaili et al., 2018](#)), \mathcal{L}_λ measures the likelihood defined by the spectral flow network between spectra λ and latent intrinsics z_I , \mathcal{L}_F is a consistency loss between the VAE (mapping between x_c and z space) and the flow network, and \mathcal{L}_D is an additional disentanglement penalty. We next define the component loss functions used in this complete objective in detail. Note that we assemble two versions of this loss, expounded in [Sec. 4.4.1](#) and [4.4.2](#), which differ in whether to use the latent intrinsics derived from x_c or λ .

4.3.1 HFVAE Loss \mathcal{L}_{HF}

Recall that our latent space $z = (z_R, z_E, z_I)$ is *structured*, in that we can partition it into three sub-vectors. Our goals are to (1) push z to follow an isotropic Gaussian latent prior and (2) force each component group $z_g, g \in \{R, E, I\}$ to be independent from the other two groups, in an information-theoretic sense. Specifically, we use *total correlation* (TC), a measure of multivariate mutual information, between latent groups to optimize disentanglement ([Watanabe, 1960](#)).

Prior work on structured disentanglement ([Esmaili et al., 2018](#)) has shown that the VAE objective can be decomposed in a hierarchical fashion via

$$\begin{aligned} \mathcal{L}_{\text{HF}}[z] = & \omega_R L_R + \beta_1 \sum_g \mathcal{I}_{\text{TC}}[z_g] + \\ & \beta_2 \sum_{d,g} \mathcal{D}_{\text{KL}}[q_\phi(z_{g,d}) || P(z_{g,d})] + \\ & \beta_3 \mathcal{I}[x_c, z] + \beta_4 \mathcal{I}_{\text{TC}}[z] \end{aligned} \quad (10)$$

where L_R denotes the reconstruction loss, the β_1 term controls the *intra*-group total correlation, the β_2 term penalizes the dimension-wise KL-divergence from the latent prior, the β_3 term controls the mutual information between x and z , and the β_4 term controls the *inter*-group total correlation. The latter term, $\mathcal{I}_{\text{TC}}(z)$, is the

most important for our application, as it encourages statistical independence between latent intrinsics and extrinsics – this is our *disentanglement* objective.

Recall that the VAE input is a quaternion q and canonical shape vector x_c , while the output are the regressions \hat{q} and \hat{x}_c . The reconstruction loss, L_R , is written as follows:

$$L_R((q, x_c), (\hat{q}, \hat{x}_c)) = \frac{\|x_c - \hat{x}_c\|_2^2}{n \mathbb{E}[\|x_c\|_2^2]} + \omega_q d_q(q, \hat{q}), \quad (11)$$

where $n = \dim(x_c)$, the expected norm $\mathbb{E}[\|x_c\|_2^2]$ normalizes for differing AEs (making hyper-parameter setting across models easier), and $d_q(q_1, q_2) = 1 - |q_1 \cdot q_2|$ is a distance metric on rotations, through unit quaternions q_1, q_2 ([Huynh, 2009](#)).

4.3.2 Flow Likelihood Loss \mathcal{L}_λ

Since f_λ is a normalizing flow network and we want to enforce \tilde{z}_I to follow the Gaussian latent prior, we can simply use the standard likelihood objective ([Papamakarios et al., 2019](#); [Kobyzev et al., 2020](#)):

$$P_\lambda(\lambda) = P_{z_I}(f_\lambda(\lambda)) |\det \mathcal{J}[f_\lambda](\lambda)|, \quad (12)$$

where P_{z_I} represents the density of an isotropic Gaussian (latent prior of z_I) and $\mathcal{J}[f]$ is the Jacobian of f . We use a weighted log-likelihood as the final loss: $\mathcal{L}_\lambda = -\omega_p \log P_\lambda(\lambda)$. This loss enforces \tilde{z}_I to follow the latent prior, as in most flow-based generative models. While it is similar to the HFVAE loss on z_I , it is an exact likelihood, rather than a lower bound.

4.3.3 Spectral Intrinsics Consistency Loss \mathcal{L}_F

We also want that the VAE encoder be consistent with the spectral flow network, so we apply a loss between the spectral and latent intrinsic space outputs:

$$\mathcal{L}_F = \omega_I \|\mu_I - \tilde{\mu}_I\|_2^2 + \omega_\lambda d_\lambda(\lambda, \hat{\lambda}). \quad (13)$$

$\tilde{\mu}_I = f_\lambda(\lambda)$, $\hat{\lambda} = g_\lambda(\mu_I)$, and d_λ is a weighted distance between spectra ([Aumentado-Armstrong et al., 2019](#)),

$$d_\lambda(\lambda, \hat{\lambda}) = \frac{1}{N_\lambda} \sum_{n=1}^{N_\lambda} \frac{|\lambda_n - \hat{\lambda}_n|}{n}, \quad (14)$$

where N_λ is the number of elements used in the spectrum. This formulation is inspired by Weyl’s estimate ([Weyl, 1911](#); [Reuter et al., 2006](#)), which posits approximately linear eigenvalue growth asymptotically. The motivation is to avoid overweighting the higher elements of the spectrum (corresponding to higher geometric frequencies and thus noisier, small-scale shape details).

4.3.4 Additional Disentanglement Losses \mathcal{L}_D

Following Aumentado-Armstrong et al. (2019), we utilize two additional losses to promote disentanglement. The first is motivated by Kumar et al. (2017), penalizing the covariance between latent groups:

$$\mathcal{L}_\Sigma = \sum_{g \neq \tilde{g}} \sum_{i,j} \left| \widehat{\Sigma}[\mu_g, \mu_{\tilde{g}}]_{i,j} \right|, \quad (15)$$

where $\widehat{\Sigma}$ is the empirical covariance matrix between latent vectors, computed per batch, and $g, \tilde{g} \in \{R, E, I\}$. The second takes advantage of the differentiable nature of the networks involved, directly penalizing the rate of change in the intrinsics as the extrinsics are varied (and vice versa). This is implemented as a penalty on the Jacobian between latent groups

$$\mathcal{L}_J = \left\| \frac{\partial \widehat{\mu}_E}{\partial \mu_I} \right\|_F^2 + \left\| \frac{\partial \widehat{\mu}_I}{\partial \mu_E} \right\|_F^2, \quad (16)$$

where $\widehat{\mu}_g = \mu_g(\widehat{x}_c)$ is the re-encoding of the reconstructed shape from the AE, $\widehat{x}_c = D_x(z_E, z_I)$, such that $\frac{\partial \widehat{\mu}_g}{\partial \mu_{\tilde{g}}} = \frac{\partial \widehat{\mu}_g}{\partial \widehat{x}_c} \frac{\partial \widehat{x}_c}{\partial \mu_{\tilde{g}}}$ for $g \neq \tilde{g}$ and μ_g is the approximate posterior mean from which z_g is sampled. Hence, the final loss term is given by $\mathcal{L}_D = \omega_\Sigma \mathcal{L}_\Sigma + \omega_J \mathcal{L}_J$.

4.4 Training Regimes

We consider two methods of training, almost independent of network architectures or hyper-parameters. The first is similar to the original Geometrically Disentangled VAE (GDVAE) model, where z_I is used for reconstruction and predicting the spectrum. This is the “flow-only” (FO) model. The second takes advantage of the shape-from-spectrum capabilities of the bijective flow mapping, using $\tilde{\mu}_I = f_\lambda(\lambda)$ for reconstruction (which does not depend on x_c), and encouraging $\mu_I(x_c)$ to be close to $\tilde{\mu}_I$. We refer to these models as **GDVAE-FO** and **GDVAE++**, respectively. Notice that the latter approach more stringently separates extrinsics and intrinsics, as the decoder has more limited access to extrinsics from $f_\lambda(\lambda)$, as opposed to using x_c . We visualize the two pathways in Fig. 8.

4.4.1 GDVAE-FO Loss

The “flow-only” model is most similar to the prior GDVAE model (Aumentado-Armstrong et al., 2019). We want the encoded intrinsic shape vector $\mu_I(x_c)$ to hold as much information as possible about the spectrum. This is accomplished through the diffeomorphic mapping to λ and the spectral losses in \mathcal{L}_F . In other words, we reconstruct via $\widehat{x}_c = D_x(z_E, z_I)$ and $\widehat{\lambda} = g_\lambda(\mu_I)$. The

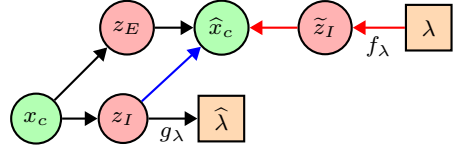


Fig. 8 Diagram of VAE mappings, depicting the ability to use latent intrinsics derived from x_c versus λ . Black lines indicate mappings always run in training. The blue arrow is used when predicting the latent reconstruction from x_c rather than λ , which is useful at inference time (when λ may not be known) and for the GDVAE-FO training scheme (see Sec. 4.4). The red arrows depict using latent intrinsics directly procured from the LBOS λ , as in the GDVAE++ training scheme.

disentanglement losses \mathcal{L}_{HF} and \mathcal{L}_D are computed with μ_I .

4.4.2 GDVAE++ Loss

For the GDVAE++ loss, we use the known spectrum to compute the output latent shape. The idea during training is to enforce the latent intrinsics used for reconstruction (in this case, \tilde{z}_I) to *only* hold intrinsic geometry (using $f_\lambda(\lambda)$), and push z_I (inferred from x_c) to be close to it. Thus, $\widehat{x}_c = D_x(z_E, \tilde{z}_I)$ is used for reconstruction, where $\tilde{z}_I \sim \mathcal{N}(\tilde{\mu}_I = f_\lambda(\lambda), \tilde{\Sigma}_I(\lambda))$. In addition, the disentanglement losses \mathcal{L}_{HF} and \mathcal{L}_D are computed with $\tilde{\mu}_I$. Note that this training strategy does not preclude us from processing shapes *without* spectra at test time, which we do for our evaluations.

5 Experimental Results

5.1 Datasets

We use the same datasets as in Aumentado-Armstrong et al. (2019). Specifically, we consider MNIST (LeCun et al., 1998), SMAL (Zuffi et al., 2017), and SMPL (Loper et al., 2015). We also assemble a Human-Animal (HA) mixed dataset by combining data from SMAL and SMPL. Note that, in all cases, we perform a scalar rescaling of the dataset such that the largest bounding box length is scaled down to unit length. This scale is the same across PCs (otherwise the change in scale would affect the spectrum for each shape differently). We apply random rotations about the gravity axis (SMAL and SMPL) or the out-of-image axis (MNIST). For rotation supervision, the orientation of the raw data is treated as canonical. See Appendix Sec. C for additional dataset details.

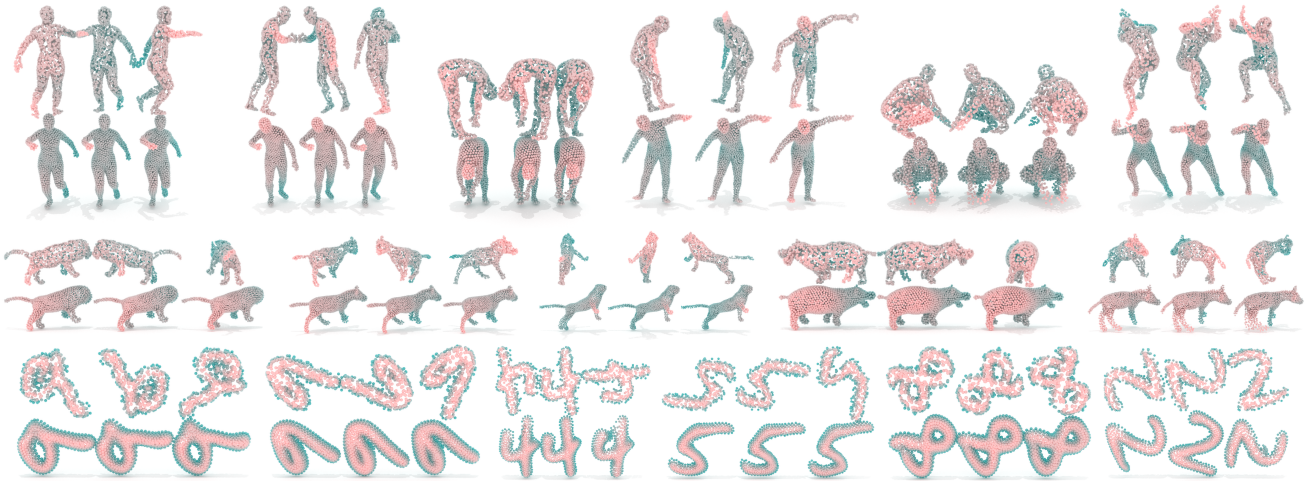


Fig. 9 Example AE reconstructions and rigid canonicalizations of input point clouds. Per inset, the top row shows input point clouds P under random rotations, while the bottom row displays the resulting canonical decodings P_c . Colors indicate depth. Architectures used are SMPL-FTL-S, SMAL-FTL-S, and MNIST-FTL-U, respectively (see Table 1). Since MNIST is unsupervised, we rotate the canonical output by a constant rotation for visualization purposes. In particular, notice that the first two MNIST insets (“9” and “6”) are rotated to match (which would be incorrect in the supervised case). We show some failure cases in the last column of each row: for SMPL, the pose (e.g., arms) is incorrectly reconstructed; for SMAL, the hind-legs of the third canonical PC does not match its counterparts, though the overall pose does; for MNIST, the canonical decoding simply fails to match across rotations. Note that we show additional reconstructions (through the VAE) in Fig. 11.

5.2 Autoencoder Results

Our AE is designed to factorize out rigid pose, as well as encode a complete representation of a canonical shape. In Fig. 9, we show example reconstructions, as well as the canonicalization capability of the model. In Fig. 10, we show latent embeddings of the shape representations x_c across different rotations of input shapes. The results show that the AE is not only able to accurately reconstruct the inputs, but also correctly derotate the canonical PCs in 3D, and that the encodings are close to being orientation invariant in the latent space.

Quantitatively, we evaluate our autoencoders on (1) reconstruction capability and (2) rotation invariance in their representation. Reconstruction quality is computed with the standard Chamfer distance between the output PC and a uniform random sampling from the raw shape mesh. We average over five randomly rotated copies of the test set.

Rotation invariance is assessed with two measures. The first is in 3D space, and checks that canonicalizations of the same PC under different rotations are close (according to the Chamfer distance between PCs):

$$\mathcal{C}_{3D} = \frac{1}{M_R} \sum_{i=1}^{m_R} \sum_{j \neq i} d_C(D(E(P)), P), \quad (17)$$

where m_R is the number of random copies we use for evaluation and M_R is the number of pairs tested.

The second measure is in the latent canonical shape space (i.e., x_c). Since latent distances are less meaningful

(e.g., dimensions may have very different scales) and will differ across AEs, we choose to measure performance by *clustering quality*. Ideally, a representation that canonicalizes an input shape should map rotated copies of a given PC to the same latent encoding – exactly fulfilling this would make it *rotation invariant*. Hence, we create rotated copies of many input shapes, encode them, and then cluster in the AE embedding space. We expect that rotated copies of the same instance should cluster together; hence, we treat instance identity as a ground truth cluster label and use Adjusted Mutual Information (AMI) to measure quality (Vinh et al., 2010). An AMI of 1 indicates perfect matching of the predicted and real partitions, while an AMI of 0 is the expected value of a random clustering. We average AMIs over clusterings obtained from different random sample sizes (i.e., the number of unique shapes duplicated and clustered). The resulting “area-under-the-curve”-like latent space clustering metric for rotational invariance is denoted \mathcal{C}_X . See Appendix Sec. B.1 for additional details.

The original GDVAE model (Aumentado-Armstrong et al., 2019) was trained on limited angles of rotation about the canonical one, since otherwise reconstruction quality was degraded but in this work we always consider full rotation about a single axis. Despite the fact that two models use essentially the same architectural components, our AE is better able to obtain canonical orientations, while maintaining reconstruction quality.

The results in Table 1 show a few patterns between the AE types. First, we find that the FTL-based AE

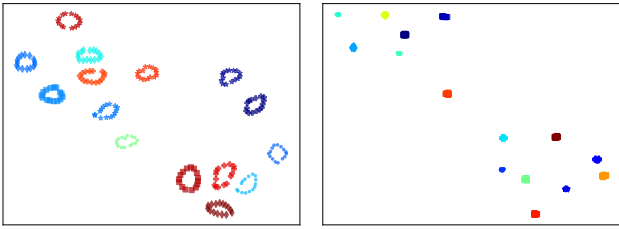


Fig. 10 Latent rotational invariance via t-sne plots of x_c vector embeddings. Plots are done with the HA-FTL-U (left) and HA-STD-U (right) models, respectively (see Table 1). Colors denote a single shape; markers with the same color are rotations of that single shape. Marker types are only meant to help tell apart shapes with similar colors. Notice the non-FTL (STD) architecture gives a tighter latent invariance.

Table 1 AE evaluation on held-out test data. Metrics (left to right) refer to the Chamfer distance in reconstructions and the rotational consistency measures (in 3D and x_c -space, respectively). HA is the humans and animals dataset (SMPL+SMAL). For each model, STD and FTL refer to the type of AE architecture, and U and S denote the use (S) or lack of (U) rotational supervision. For the HA dataset, a/b denote the values on the SMAL and SMPL test sets, respectively. Also, note that, for HA, SMPL shapes are scaled with the SMAL maximum bounding box length; therefore, we scale the Chamfer distances in the evaluations to match the other SMPL models, to make them comparable. \uparrow (\downarrow) means the higher (lower) the better.

Dataset	Model	$d_C(P, \hat{P}) \downarrow$	$C_{3D} \downarrow$	$C_X \uparrow$
MNIST	STD-U	1.19	1.57	0.92
	FTL-U	0.94	2.73	0.65
SMAL	STD-S	0.35	0.03	0.97
	FTL-S	0.10	0.14	0.93
	STD-U	0.29	0.01	0.97
	FTL-U	0.10	0.21	0.88
SMPL	STD-S	0.34	0.03	0.97
	FTL-S	0.19	0.30	0.71
	STD-U	0.23	0.05	0.97
	FTL-U	0.18	0.45	0.70
HA	STD-S	0.36/0.44	0.03/0.05	0.97/0.97
	FTL-S	0.11/0.19	0.24/0.22	0.66/0.62
	STD-U	0.33/0.34	0.02/0.06	0.97/0.97
	FTL-U	0.11/0.19	0.20/0.20	0.72/0.66

has superior reconstruction quality, while the STD AE has much better rotation invariance. Second, the difference between the unsupervised and supervised scenarios is relatively smaller, with the unsupervised reconstruction quality being slightly better than the supervised, whereas the supervised case has superior rotation invariance. Finally, performance on the HA dataset (which includes SMAL and SMPL data) is only slightly degraded compared to the per-category models (more so for FTL than STD).

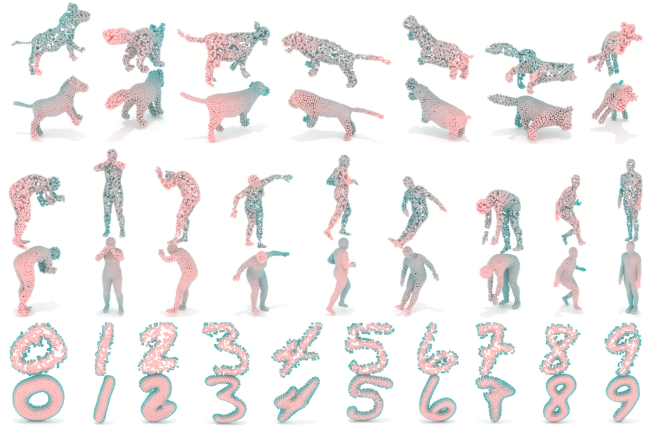


Fig. 11 Reconstructions through the VAE. Odd rows are inputs; even rows are reconstructions. Since the model is learned in x_c -space, reconstruction error manifests as shapes being valid, but slightly off in shape and/or pose (e.g., left-most and right-most insets of top row). All models use the FTL-based AE. See Fig. 9 for qualitative example reconstructions through only the AE. Note that inputs and outputs have the same number of points.



Fig. 12 Random sample generations from the VAE. All models use the FTL-based AE. Note that the MNIST model was trained on digits at all orientations and thus should output samples at any orientation (as for SMAL and SMPL). Rows: SMAL, SMPL, MNIST, and HA.

5.3 Latent Variational Autoencoder Results

We evaluate our VAE model on three main criteria: (1) representational fidelity, (2) generative modeling, and (3) intrinsic-extrinsic disentanglement. Representational fidelity is captured simply as the reconstruction error, measured via the Chamfer distance between input and output (see Fig. 11 for qualitative examples). To assess generative modeling capability, we utilize the coverage and fidelity metrics (Achlioptas et al., 2017), which examine how well samples from our VAE represent a held-out test set. In addition, utilizing our flow network, we can measure the quality of spectrum generation using the standard log-likelihood. Finally, using the known ground truth intrinsics and extrinsics of our synthetic SMAL and SMPL data, we can measure disentanglement quality via a pose-aware retrieval task. We discuss our results and the details of these metrics in the fol-

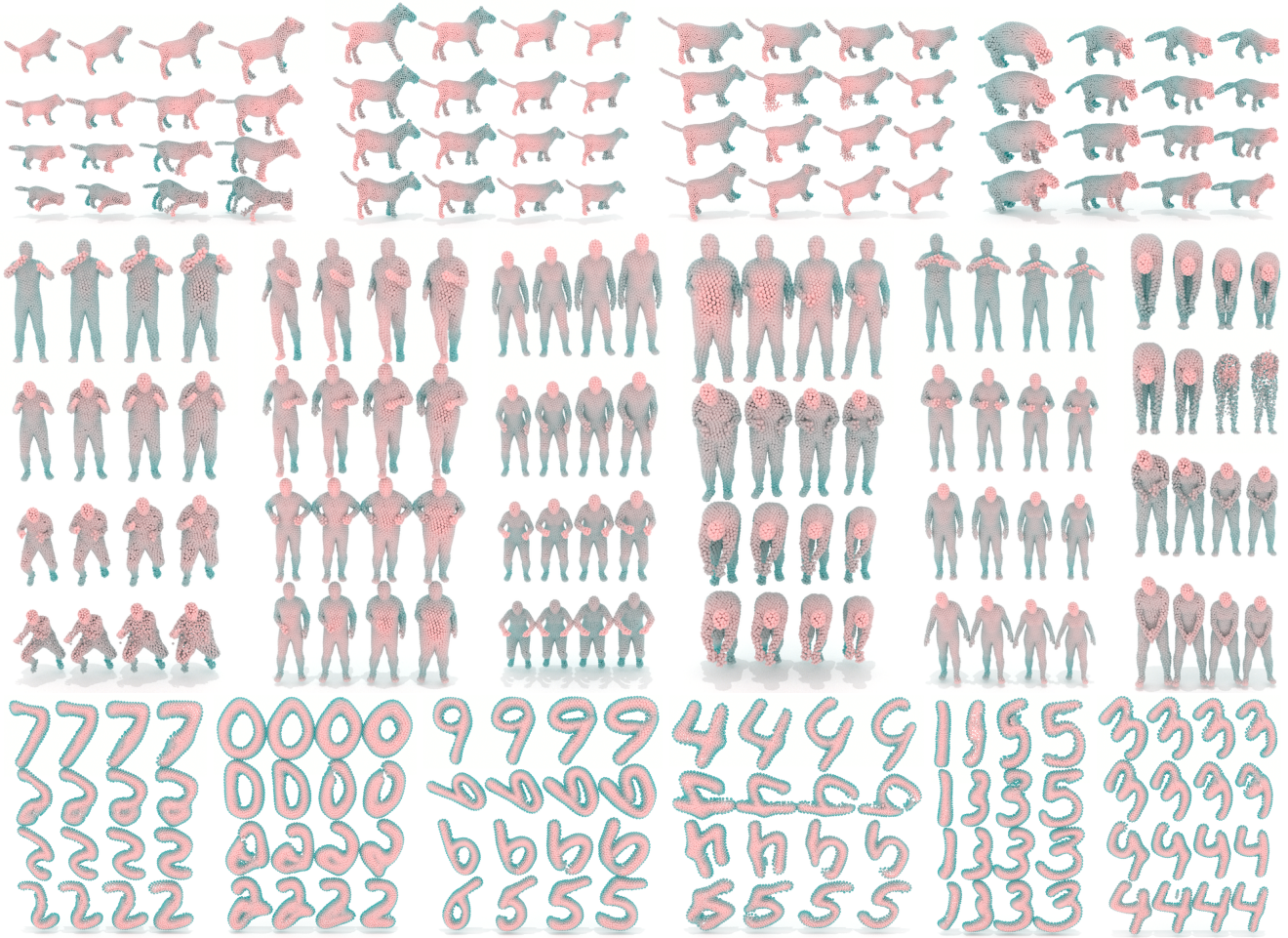


Fig. 13 Intrinsic-extrinsic latent space interpolations using the disentangled VAE representation. In each 4×4 panel, top-left and bottom-right shapes are reconstructions of real inputs. Along the horizontal axis, we interpolate along the intrinsics (z_I), whereas we do so for the extrinsics (z_E) along the vertical axis. Notice that the bottom-left and top-right shapes are *pose transfers*, for which one of the latent factors is exchanged, while the other remains unchanged. SMAL and SMPL shapes are shown in the learned canonical orientation (using FTL-S); for MNIST only (using FTL-U), we interpolate the estimated AE rotation encodings q as well, via sleping the quaternions (Shoemake, 1985) between the two inputs along with the extrinsics (i.e., along the vertical axis).

lowing sections. Table 2 shows our quantitative results on metrics for all of these criteria.

5.3.1 Generative Modeling

We measure generative modeling quality using the metrics introduced by Achlioptas et al. (2017). Consider two sets of PC shapes: ζ_G , a random set of generated samples, and ζ_R , a set of real PCs. Note that generations are computed via $P = D(D_x(z_E, z_I))R(D_q(z_R)) \in \zeta_G$, where $z_R, z_E, z_I \sim \mathcal{N}(0, I)$ (see Sec. 3.1 and 4.2.1). Briefly, we consider two measures: *coverage*, which checks how well ζ_G covers the modes of ζ_R (a proxy for set diversity), and *fidelity*, which considers how faithful each element in ζ_G is to its closest counterpart in ζ_R (a proxy for per-element realism). Coverage is computed by matching each $Q \in \zeta_G$ to its closest PC in ζ_R , and counting the

percent of PCs chosen (matched) in ζ_R (high coverage meaning most of the PCs in ζ_R are represented in ζ_G). Fidelity (also called minimum matching distance) is computed by matching each $P \in \zeta_R$ to its closest pair in ζ_G , taking the Chamfer distance between them, and averaging these distances over the dataset. Fidelity is needed because coverage does not measure the quality of the matchings (e.g., low quality PCs could be used to cover a given real PC). Matching is always computed as the minimum Chamfer distance. Similar to (Achlioptas et al., 2017), we generate synthetic set five times larger than the held-out test set, and report the average of running the same evaluation twice. Quantitative scores are displayed in Table 2. For qualitative visualizations, random sample generations are shown in Fig. 12.



Fig. 14 Example retrievals using the disentangled factors of the GDVAE++ latent representation. Shapes are in order of latent similarity from left to right). SMAL, SMPL, and MNIST use FTL-S, FTL-S, and FTL-U AE models, respectively. For SMAL and SMPL, notice that z_E retrieves a variety of animals/body types in the same articulated pose, while z_I retrieves the same animal/body type in an array of different non-rigid poses. Though MNIST does not have a natural sense of articulation, notice that the extrinsic retrievals tend to have the same digit identity, but vary most noticeably in thickness (which is a non-isometric alteration). In contrast, digits retrieved via z_I appear to be bent largely isometrically; that is, “wiggled” around in a way that preserves the metric tensor (and the distribution of geodesic distances among points) – see the “8” digit. For the “6”, notice that it retrieves several “9” digits, showing its blindness to orientation, as well as two “5” shapes that were “thickened” sufficiently in a manner similarly to the query.

Separately, our flow model f_λ provides a generative model on LBOSs. Using its bijectivity, we can directly compute the log-likelihood. This measures how well our spectral encoder maps real spectra into the Gaussian latent space of the intrinsics.

Looking at Table 2, we can see that the GDVAE++ and GDVAE-FO score similarly for generative fidelity and coverage, and obtain mixed results on $\log P_\lambda(\lambda)$ (the FO method performs better or similar with the FTL AE, but worse with the STD AE), but GDVAE-FO always has better reconstruction results. In terms of AE type, results are mixed, though the FTL approach does tend to have slightly better coverage and worse fidelity. We discuss results related to disentanglement quality in the next subsection.

5.3.2 Shape-Pose Disentanglement

To measure disentanglement quantitatively, we rely on a *pose-aware* retrieval task in which ground truth continuous values for intrinsics and extrinsics are known.

We start with a set of shapes (SMAL or SMPL) for which parameters for intrinsic shape β and extrinsic pose θ are known. These shapes *were not* used in training. Let point cloud P_i have parameters (β_i, θ_i) . Using our model, we encode P_i into a latent representation $\rho_i \in \{x_c(P_i), z(P_i), z_E(P_i), z_I(P_i)\}$. We then measure distances between representations as $d_\rho(P_i, P_j) = \|\rho_i - \rho_j\|_2^2$, and rank the retrieved shapes based on ρ_i . We measure the retrieval quality for a retrieved PC, P_j , using query P_i , by separately checking how well the intrinsic shape and non-rigid pose match. This is done by comparing the query ground truth parameters, (β_i, θ_i) , to (β_j, θ_j) , from the retrieved shape.

Table 2 VAE Evaluation on held-out test data. The first three columns denote the dataset, the VAE type, and the AE type (S and U mean supervised and unsupervised, respectively). GDVAE-FO means using the x_c -derived latent intrinsics (as opposed to the λ -derived one) in training; PCLBO and NCNJ denote using point cloud-based LBOs and ablating the \mathcal{L}_D loss, respectively. The five right-most columns are evaluation metrics, considering reconstruction (d_C), generative modelling (Fidelity, Coverage, and $\log P_\lambda(\lambda)$), and unsupervised disentanglement (\mathcal{S}). See Sec. 5.3.4 and 5.3.3 for additional details on the alterations (PCLBO and NCNJ), Sec. 4.4 for the difference between GDVAE++ and GDVAE-FO, Sec. 5.3.1 for the generative modelling metrics, and Sec. 5.3.2 for the scalar disentanglement measure. For the HA dataset, we show A/B as the scores on the SMAL and SMPL test sets, respectively, and we also scale Chamfer distances for the HA dataset to make them comparable across datasets, as in Table 1. We see that the GDVAE++ model obtains much better disentanglement scores than the GDVAE model (across SMAL, SMPL, and HA), while GDVAE-FO does significantly worse. In terms of retrieval quality, using the PCLBO degrades performance, but it stays above the GDVAE as well, while ablating \mathcal{L}_D (the NCNJ scenario) worsens performance on SMPL but has little effect for SMAL.

Dataset	VAE Model	AE Model	$d_C(P, \hat{P}) \downarrow$	Fidelity \downarrow	Coverage \uparrow	$\log P_\lambda(\lambda) \uparrow$	$\mathcal{S} \uparrow$	
SMAL	GDVAE++	STD-S	0.56	0.83	0.77	-121.60	2.07	
		FTL-S	0.40	1.20	0.62	-144.17	2.12	
		STD-U	0.39	0.68	0.66	-114.73	2.02	
		FTL-U	0.73	0.99	0.75	-135.21	2.07	
	GDVAE-FO	STD-S	0.48	0.81	0.72	-147.60	0.49	
		FTL-S	0.24	0.90	0.73	-143.39	0.43	
	GDVAE++ (PCLBO)	STD-S	0.51	0.89	0.65	-116.62	1.83	
		FTL-S	1.05	1.09	0.65	-111.12	1.11	
	GDVAE++ (NCNJ)	STD-S	0.44	1.20	0.47	-151.32	2.14	
		FTL-S	0.34	1.09	0.57	-196.15	2.06	
	SMPL	GDVAE++	STD-S	0.50	1.21	0.73	-131.82	2.58
			FTL-S	0.38	1.38	0.80	-137.06	2.46
STD-U			0.36	1.11	0.67	-151.74	2.46	
FTL-U			0.43	1.38	0.80	-135.45	1.93	
GDVAE-FO		STD-S	0.43	1.21	0.65	-232.73	0.32	
		FTL-S	0.26	1.33	0.79	-94.65	0.64	
GDVAE++ (PCLBO)		STD-S	0.53	1.16	0.80	-164.64	1.43	
		FTL-S	0.37	1.47	0.77	-145.43	1.35	
GDVAE++ (NCNJ)		STD-S	0.43	1.36	0.54	-178.26	2.01	
		FTL-S	0.36	1.44	0.58	-123.40	2.24	
HA		GDVAE++	STD-S	0.54/0.64	0.89/1.32	0.63/0.68	-130.13/-125.44	1.86/1.92
			FTL-S	0.40/0.65	1.06/1.54	0.74/0.59	-117.82/-108.69	1.72/1.83

We compute the distance between these parameters, as the mean squared error between β values and the average rotational distance d_q across corresponding joint rotations, denoted E_β and E_θ , respectively. Note that we normalize E_β and E_θ by the mean pairwise error across the dataset for each measure, so that it is relative to the expected error of a *uniformly random* retrieval algorithm (1 corresponds to random retrieval, while 0 implies obtaining the same parameter set). More specifically, we use the encoding(s) ρ of a PC P , to retrieve the three closest shapes (in terms of d_ρ), and compute the errors E_β and E_θ averaged over these three retrievals, to obtain two errors per shape. For a fixed encoding type $\rho \in \{x_c(P), z(P), z_E(P), z_I(P)\}$, we get a final error by averaging over an entire held-out test set. Hence, we obtain two scalars E_β and E_θ for each choice of ρ .

We then convert these errors into scores, $s_\psi(\rho) = 1 - E_\psi(\rho)$, where $\psi \in \{\theta, \beta\}$. We expect using z_E for

retrieval (i.e., as ρ) to result in a *high* intrinsic error $E_\beta(z_E)$ (*low* score $s_\beta(z_E)$), but a *low* extrinsic error $E_\theta(z_E)$ (*high* score $s_\theta(z_E)$). Using z_I should result in the converse: a *high* intrinsic score $s_\beta(z_I)$ and a *low* extrinsic score $s_\theta(z_I)$. We expect retrieval with x_c or z to obtain high scores for both parameters.

Lastly, we wish to have a final scalar score that expresses the quality of disentanglement obtained by the model. Notice that s_β and s_θ are normalized with respect to a random retriever, but are still not comparable (as the errors are originally different units and at different scales). Hence we compute $\hat{s}_\psi(z_g) = s_\psi(z_g)/s_\psi(x_c)$, with $z_g \in \{z, z_E, z_I\}$, normalizing beta and theta retrievals to be in approximately the “same” units (both are errors relative to the AE).

With these normalizations, we make the following interpretations: $\hat{s}_\psi(z_g) = 0$ means that using z_g to retrieve shapes is no better (with respect to ψ) than random re-

trieval. In contrast, $\widehat{s}_\psi(z_g) = 1$ implies that z_g performs just as well as using x_c ; this comparison is relevant, because the AE limits the amount of information available to the VAE. Higher scores (e.g., $\widehat{s}_\psi(z_g) = 2$) imply that z_g performs $\widehat{s}_\psi \times$ better than x_c (specifically for retrieving pose alone, when $\psi = \theta$, or intrinsic shape alone, when $\psi = \beta$).

Our normalized retrieval scores $\widehat{s}_\psi(z_g)$ are then used to compute a final disentanglement scalar

$$\mathcal{S} = \widehat{s}_\beta(z_I) + \widehat{s}_\theta(z_E) - \widehat{s}_\beta(z_E) - \widehat{s}_\theta(z_I). \quad (18)$$

Higher \mathcal{S} requires accurate extrinsics-based retrieval in terms of pose (high $\widehat{s}_\theta(z_E)$), but poor retrieval (when using z_E) with respect to intrinsics β (low $\widehat{s}_\beta(z_E)$); at the same time, it requires the opposite performance for the latent intrinsics z_I . Note that random retrieval performance results in all terms being zero (hence $\mathcal{S} = 0$); however, one *also* obtains $\mathcal{S} = 0$ if performance for each term is the same as the AE (since all four terms would be one). In other words, good performance retrieving intrinsics (extrinsics) with z_I (z_E) will be cancelled out by good performance retrieving extrinsics (intrinsics) with z_I (z_E). This shows that a high \mathcal{S} requires disentanglement between z_E and z_I .

Disentanglement scores are reported in Table 2. Note that retrieval scores \mathcal{S} are 1.08 and 1.04, for SMAL and SMPL respectively, in the original GDVAE work. As such, the GDVAE++ model obtains significantly superior disentanglement scores across both datasets (including from the HA model) – around double the score of the original model.

From Table 3, we also observe the superiority of $\tilde{z}_I = f_\lambda(\lambda)$ over z_I in retrieving intrinsics, suggesting one should use the spectrum directly when it is available for such a task, though the raw spectrum λ cannot be used for other tasks (e.g., smooth interpolation, generation, or same-pose-different-shape retrieval).

Qualitatively, we can assess disentanglement by looking at interpolations within the factorized latent space (shown in Fig. 13). The interpolation plots also show examples of *pose transfers* (upper-right and lower left corners per inset). For SMAL and SMPL, one can see that the network correctly disentangles articulated pose and shape. For MNIST, where an obvious notion of articulation is not present, moving in z_I tends to change digit thickness or allow large-scale shape alterations, while changing z_E approximately leaves geodesic distance distributions unchanged (though it can change major factors, like topology).

We can also consider the retrievals qualitatively based on the disentangled latent vectors. Fig. 14 shows what shapes the networks think are most similar to each

query, in terms of intrinsics versus extrinsics. We observe that z_E is able to retrieve very similar articulations across many animals and/or human body types, while z_I correctly retrieves similar shapes without regard for non-rigid pose. For MNIST, retrieval with z_E tends to mostly return the same digit with differing thicknesses, while retrieval with z_I also largely results in the same digit, but under isometric (non-geodesic-altering) deformations. There are some exceptions to these, such as the nines retrieved by the z_I from the six (as the spectrum is unaffected by rotation) or the fives there (potentially due to the closeness of the end of the last stroke in the five to the upper portion of the digit, as well as its thickness, leading to greater intrinsic similarity). The ones retrieved for the eight by z_E are less obvious to interpret; they may be due to the low dimensionality of z_E or the similarity of ones to thin eights.

5.3.3 Spectral Robustness

Although we use point clouds as our shape representation, our spectra are computed on the mesh forms of the shapes, via the cotan weight formulation (Meyer et al., 2003). For completeness, we therefore also investigated the effect of computing the spectra directly on our subsampled point clouds. This mesh-to-point-cloud conversion process introduces several additional sources of noise: for instance, parts far in geodesic distance may be close in Euclidean space (altering the LBO), and the subsampling of the surface (our PCs being smaller than the number of vertices in SMPL and SMAL) also introduces noise. Hence, we expect results to be degraded, compared to the prior section. For computing the point cloud LBO (PCLBO), we use the robust “tufted” Laplacian operator (Sharp and Crane, 2020).

The scalar disentanglement results are shown in Table 2. While the scores do decrease overall, they are still superior to the scores from the original GDVAE (which used mesh-derived LBOs) and the GDVAE-FO models. From Table 3, we see that two major terms are degraded in the PCLBO case, likely due to noise in the estimated LBOs. First, the ability of z_I to capture intrinsics, $\widehat{s}_\beta(z_I)$, declines; second, removal of intrinsic information from z_E is degraded, captured by $\widehat{s}_\beta(z_E)$ being too high (especially for SMPL).

5.3.4 Ablations

Lastly, we consider the effect of ablating two aspects of the model: the additional disentanglement loss \mathcal{L}_D and the shape-from-spectrum reconstruction used in the GDVAE++ training.

Table 3 Retrieval scores. All models use the GDVAE++ training regime. \uparrow (\downarrow) means the higher (lower) the better. See Sec. 5.3.2 for additional details.

Data	Model	\widehat{s}_ψ	$z \uparrow$	z_E	z_I	\widetilde{z}_I
SMAL	STD-S	\widehat{s}_β	1.46	0.23 \downarrow	1.63 \uparrow	2.04 \uparrow
		\widehat{s}_θ	0.69	0.83 \uparrow	0.16 \downarrow	0.08 \downarrow
	FTL-S	\widehat{s}_β	1.52	0.13 \downarrow	1.66 \uparrow	1.77 \uparrow
		\widehat{s}_θ	0.61	0.68 \uparrow	0.11 \downarrow	0.12 \downarrow
	STD-U	\widehat{s}_β	1.35	0.19 \downarrow	1.56 \uparrow	1.90 \uparrow
		\widehat{s}_θ	0.73	0.79 \uparrow	0.15 \downarrow	0.06 \downarrow
	FTL-U	\widehat{s}_β	1.54	0.15 \downarrow	1.77 \uparrow	1.99 \uparrow
		\widehat{s}_θ	0.63	0.66 \uparrow	0.21 \downarrow	0.18 \downarrow
	(PCLBO)	\widehat{s}_β	1.15	0.16 \downarrow	1.30 \uparrow	2.00 \uparrow
		\widehat{s}_θ	0.74	0.89 \uparrow	0.20 \downarrow	0.04 \downarrow
	(PCLBO)	\widehat{s}_β	0.74	0.25 \downarrow	0.96 \uparrow	1.84 \uparrow
		\widehat{s}_θ	0.56	0.62 \uparrow	0.21 \downarrow	0.09 \downarrow
(NCNJ)	\widehat{s}_β	1.38	0.20 \downarrow	1.60 \uparrow	1.93 \uparrow	
	\widehat{s}_θ	0.73	0.91 \uparrow	0.17 \downarrow	0.07 \downarrow	
(NCNJ)	\widehat{s}_β	1.55	0.19 \downarrow	1.69 \uparrow	1.91 \uparrow	
	\widehat{s}_θ	0.73	0.70 \uparrow	0.13 \downarrow	0.07 \downarrow	
SMPL	STD-S	\widehat{s}_β	0.72	0.12 \downarrow	1.97 \uparrow	1.73 \uparrow
		\widehat{s}_θ	0.94	0.93 \uparrow	0.20 \downarrow	0.34 \downarrow
	FTL-S	\widehat{s}_β	0.85	0.12 \downarrow	1.78 \uparrow	2.11 \uparrow
		\widehat{s}_θ	0.90	0.95 \uparrow	0.15 \downarrow	0.25 \downarrow
	STD-U	\widehat{s}_β	0.65	0.06 \downarrow	1.95 \uparrow	1.80 \uparrow
		\widehat{s}_θ	0.90	0.87 \uparrow	0.30 \downarrow	0.29 \downarrow
	FTL-U	\widehat{s}_β	0.97	0.30 \downarrow	1.58 \uparrow	2.03 \uparrow
		\widehat{s}_θ	0.87	0.89 \uparrow	0.24 \downarrow	0.28 \downarrow
	(PCLBO)	\widehat{s}_β	0.42	0.23 \downarrow	0.90 \uparrow	1.74 \uparrow
		\widehat{s}_θ	0.93	0.91 \uparrow	0.14 \downarrow	0.31 \downarrow
	(PCLBO)	\widehat{s}_β	0.71	0.43 \downarrow	1.09 \uparrow	2.01 \uparrow
		\widehat{s}_θ	0.91	0.91 \uparrow	0.21 \downarrow	0.30 \downarrow
(NCNJ)	\widehat{s}_β	1.26	0.24 \downarrow	1.63 \uparrow	2.23 \uparrow	
	\widehat{s}_θ	0.74	0.96 \uparrow	0.34 \downarrow	0.38 \downarrow	
(NCNJ)	\widehat{s}_β	1.35	0.22 \downarrow	1.66 \uparrow	2.24 \uparrow	
	\widehat{s}_θ	0.77	0.96 \uparrow	0.15 \downarrow	0.32 \downarrow	

First, we investigate the utility of the additional disentanglement penalties. By removing these losses, we have no covariance and no Jacobian terms; we denote this scenario NCNJ. For SMAL, the disentanglement scores seem unaffected by this ablation; however, it seems to have introduced a trade-off between reconstruction and generative modelling errors, with d_C improving but coverage and $\log P_\lambda(\lambda)$ degrading. For SMPL, NCNJ results in degradations in the disentanglement and generative coverage scores. Note that since the VAE prior is Gaussian, it presupposes latent independence (Higgins et al., 2017); hence, disentanglement is likely to affect the prior fitting (and hence generative quality and $\log P_\lambda(\lambda)$ as well).

Second, we look at the effectiveness of the “flow-only” training approach, where we do not perform latent shape-from-spectrum during training to perform reconstruction, and instead only use the direct encoding of the AE output. We find that this incurs the most significant degradation in terms of disentanglement score, across both datasets, showing the importance of using the uncontaminated spectrum for training, rather than relying on the \mathcal{L}_F to force z_I to carry only intrinsic information. One may notice that, even though GDVAE-FO is similar to the GDVAE model (Aumentado-Armstrong et al., 2019)¹, it has a much lower disentanglement score. This can be partly explained by the increase in dimensionality of the latent intrinsics, as the newer model has a 4-5 times larger $\dim(z_I)$ than the original GDVAE.

6 Discussion

In this work, we have devised a method for separating the deformation space of an object into rigid orientation, non-rigid extrinsic pose, and intrinsic shape. We require no information other than the geometry of the shapes themselves (i.e., no labels or correspondences). Our method relies on the isometry invariance of the LBOS, which can be estimated from the geometry directly, and uses disentanglement techniques to partition the latent space of a generative model into these independent components.

Our results show that we have significantly improved on the GDVAE model (Aumentado-Armstrong et al., 2019). Firstly, we are able to handle larger orientation changes with far better robustness in both the 3D data space and latent space (see Sec. 5.2), utilizing rotational invariance techniques that do not rely on a specific feature extraction or neural architecture. Secondly, we obtain nearly double the quantitative disentanglement score, for data from both SMAL and SMPL, using our GDVAE++ training scheme (see Sec. 5.3.2). We also examined the ability of the model to generate novel shape samples, its capacity to smoothly and independently control latent shape and non-rigid pose (see Fig. 13), and the effect of several ablations and modifications of the model.

For future work, we expect research on *localized* spectral geometry (Neumann et al., 2014; Melzi et al., 2018), LBO modifications (Choukroun et al., 2018; Andreux et al., 2014), and *extrinsic* spectral shape (Liu et al., 2017; Ye et al., 2018; Wang et al., 2017) to be potentially useful. Furthermore, our formulation is readily applicable to other 3D shape modalities (e.g., tetrahedral meshes or implicit fields), as the only elements of our

¹ Except for the flow network and altered AEs.

architecture that would require alteration are the AE encoders (E_r and E_x) and decoder (D), provided one has a way to estimate the LBOS. Our VAE model is also agnostic to the neural architecture of the AE. Hence, our approach could be used in conjunction with other methods for factorizing deformations. Lastly, our method can also be utilized for applications in computer vision. For instance, it can be used for controllable shape generation or manipulation, for regularizing visual inference (e.g., by acting as a prior on expected deformation types), or for pose-aware shape retrieval.

In general, we hope that our model can serve as an interpretable unsupervised prior for understanding shape deformations.

References

- Achlioptas P, Diamanti O, Mitliagkas I, Guibas L (2017) Learning representations and generative models for 3d point clouds. arXiv preprint arXiv:170702392
- Andreux M, Rodola E, Aubry M, Cremers D (2014) Anisotropic laplace-beltrami operators for shape analysis. In: European Conference on Computer Vision, Springer, pp 299–312
- Aubry M, Schlickewei U, Cremers D (2011) The wave kernel signature: A quantum mechanical approach to shape analysis. In: Computer Vision Workshops (ICCV Workshops), 2011 IEEE International Conference on, IEEE, pp 1626–1633
- Aumentado-Armstrong T, Tsogkas S, Jepson A, Dickinson S (2019) Geometric disentanglement for generative latent shape models. In: Proceedings of the IEEE International Conference on Computer Vision, pp 8181–8190
- Ba JL, Kiros JR, Hinton GE (2016) Layer normalization. arXiv preprint arXiv:160706450
- Baek SY, Lim J, Lee K (2015) Isometric shape interpolation. *Computers & Graphics* 46:257–263
- Basset J, Wuhler S, Boyer E, Multon F (2020) Contact preserving shape transfer: Retargeting motion from one shape to another. *Computers & Graphics*
- Bengio Y, Courville A, Vincent P (2013) Representation learning: A review and new perspectives. *IEEE transactions on pattern analysis and machine intelligence* 35(8):1798–1828
- Berkiten S, Halber M, Solomon J, Ma C, Li H, Rusinkiewicz S (2017) Learning detail transfer based on geometric features. In: Computer Graphics Forum, Wiley Online Library, vol 36, pp 361–373
- Boscaini D, Eynard D, Kourounis D, Bronstein MM (2015a) Shape-from-operator: Recovering shapes from intrinsic operators. In: Computer Graphics Forum, Wiley Online Library, vol 34, pp 265–274
- Boscaini D, Masci J, Melzi S, Bronstein MM, Castellani U, Vandergheynst P (2015b) Learning class-specific descriptors for deformable shapes using localized spectral convolutional networks. In: Computer Graphics Forum, Wiley Online Library, vol 34, pp 13–23
- Bronstein AM, Bronstein MM, Guibas LJ, Ovsjanikov M (2011) Shape google: Geometric words and expressions for invariant shape retrieval. *ACM Transactions on Graphics (TOG)* 30(1):1
- Chen C, Li G, Xu R, Chen T, Wang M, Lin L (2019a) Clusternet: Deep hierarchical cluster network with rigorously rotation-invariant representation for point cloud analysis. In: Proceedings of the IEEE Conference on Computer Vision and Pattern Recognition, pp 4994–5002
- Chen X, Chen B, Mitra NJ (2019b) Unpaired point cloud completion on real scans using adversarial training. arXiv preprint arXiv:190400069
- Choukroun Y, Shtern A, Bronstein AM, Kimmel R (2018) Hamiltonian operator for spectral shape analysis. *IEEE transactions on visualization and computer graphics*
- Chua CS, Jarvis R (1997) Point signatures: A new representation for 3d object recognition. *International Journal of Computer Vision* 25(1):63–85
- Cohen TS, Geiger M, Köhler J, Welling M (2018) Spherical cnns. arXiv preprint arXiv:180110130
- Corman E, Solomon J, Ben-Chen M, Guibas L, Ovsjanikov M (2017) Functional characterization of intrinsic and extrinsic geometry. *ACM Transactions on Graphics (TOG)* 36(2):14
- Cosmo L, Norelli A, Halimi O, Kimmel R, Rodolà E (2020) Limp: Learning latent shape representations with metric preservation priors. arXiv preprint arXiv:200312283
- Dinh L, Sohl-Dickstein J, Bengio S (2016) Density estimation using real nvp. arXiv preprint arXiv:160508803
- Durkan C, Bekasov A, Murray I, Papamakarios G (2020) nflows: normalizing flows in PyTorch DOI 10.5281/zenodo.4296287, URL <https://doi.org/10.5281/zenodo.4296287>
- Esmaeili B, Wu H, Jain S, Bozkurt A, Siddharth N, Paige B, Brooks DH, Dy J, van de Meent JW (2018) Structured disentangled representations. arXiv preprint arXiv:180402086
- Gao L, Yang J, Qiao YL, Lai YK, Rosin PL, Xu W, Xia S (2018) Automatic unpaired shape deformation transfer. *ACM Transactions on Graphics (TOG)* 37(6):1–15
- Gebal K, Bærentzen JA, Aanæs H, Larsen R (2009) Shape analysis using the auto diffusion function. In: Computer Graphics Forum, Wiley Online Library, vol 28, pp 1405–1413

- Ghosh P, Sajjadi MS, Vergari A, Black M, Schölkopf B (2019) From variational to deterministic autoencoders. arXiv preprint arXiv:190312436
- Groueix T, Fisher M, Kim VG, Russell BC, Aubry M (2018) 3d-coded: 3d correspondences by deep deformation. In: Proceedings of the European Conference on Computer Vision (ECCV), pp 230–246
- Guo Y, Bennamoun M, Sohel F, Lu M, Wan J (2014) 3d object recognition in cluttered scenes with local surface features: a survey. *IEEE Transactions on Pattern Analysis and Machine Intelligence* 36(11):2270–2287
- Higgins I, Matthey L, Pal A, Burgess C, Glorot X, Botvinick M, Mohamed S, Lerchner A (2017) β -vae: Learning basic visual concepts with a constrained variational framework. In: International Conference on Learning Representations
- Huynh DQ (2009) Metrics for 3d rotations: Comparison and analysis. *Journal of Mathematical Imaging and Vision* 35(2):155–164
- Johnson AE, Hebert M (1999) Using spin images for efficient object recognition in cluttered 3d scenes. *IEEE Transactions on pattern analysis and machine intelligence* 21(5):433–449
- Kingma DP, Ba J (2014) Adam: A method for stochastic optimization. arXiv preprint arXiv:1412.6980
- Kingma DP, Dhariwal P (2018) Glow: Generative flow with invertible 1x1 convolutions. In: Advances in neural information processing systems, pp 10215–10224
- Kobyzev I, Prince S, Brubaker M (2020) Normalizing flows: An introduction and review of current methods. *IEEE Transactions on Pattern Analysis and Machine Intelligence*
- Kovnatsky A, Bronstein MM, Bronstein AM, Glashoff K, Kimmel R (2013) Coupled quasi-harmonic bases. In: Computer Graphics Forum, Wiley Online Library, vol 32, pp 439–448
- Kumar A, Sattigeri P, Balakrishnan A (2017) Variational inference of disentangled latent concepts from unlabeled observations. arXiv preprint arXiv:1711.00848
- LeCun Y, Bottou L, Bengio Y, Haffner P (1998) Gradient-based learning applied to document recognition. *Proceedings of the IEEE* 86(11):2278–2324
- Levinson J, Sud A, Makadia A (2019) Latent feature disentanglement for 3d meshes. arXiv preprint arXiv:1906.03281
- Lévy B (2006) Laplace-beltrami eigenfunctions towards an algorithm that understands geometry. In: Shape Modeling and Applications, 2006. SMI 2006. IEEE International Conference on, IEEE, pp 13–13
- Li J, Bi Y, Lee GH (2019) Discrete rotation equivariance for point cloud recognition. In: 2019 International Conference on Robotics and Automation (ICRA), IEEE, pp 7269–7275
- Liu HTD, Jacobson A, Crane K (2017) A dirac operator for extrinsic shape analysis. In: Computer Graphics Forum, Wiley Online Library, vol 36, pp 139–149
- Loper M, Mahmood N, Romero J, Pons-Moll G, Black MJ (2015) SMPL: A skinned multi-person linear model. *ACM Trans Graphics (Proc SIGGRAPH Asia)* 34(6):248:1–248:16
- van der Maaten L, Hinton G (2008) Visualizing data using t-sne. *Journal of machine learning research* 9(Nov):2579–2605
- MacQueen J, et al. (1967) Some methods for classification and analysis of multivariate observations. In: Proceedings of the fifth Berkeley symposium on mathematical statistics and probability, Oakland, CA, USA, vol 1, pp 281–297
- Marin R, Rampini A, Castellani U, Rodolà E, Ovsjanikov M, Melzi S (2020) Instant recovery of shape from spectrum via latent space connections. arXiv preprint arXiv:2003.06523
- Masoumi M, Hamza AB (2017) Spectral shape classification: A deep learning approach. *Journal of Visual Communication and Image Representation* 43:198–211
- Melzi S, Rodolà E, Castellani U, Bronstein MM (2018) Localized manifold harmonics for spectral shape analysis. In: Computer Graphics Forum, Wiley Online Library, vol 37, pp 20–34
- Meyer M, Desbrun M, Schröder P, Barr AH (2003) Discrete differential-geometry operators for triangulated 2-manifolds. In: Visualization and mathematics III, Springer, pp 35–57
- Narayanaswamy S, Paige B, Van de Meent JW, Desmaison A, Goodman N, Kohli P, Wood F, Torr P (2017) Learning disentangled representations with semi-supervised deep generative models. In: Advances in Neural Information Processing Systems, pp 5925–5935
- Neumann T, Varanasi K, Theobalt C, Magnor M, Wacker M (2014) Compressed manifold modes for mesh processing. In: Computer Graphics Forum, Wiley Online Library, vol 33, pp 35–44
- Ovsjanikov M, Ben-Chen M, Solomon J, Butscher A, Guibas L (2012) Functional maps: a flexible representation of maps between shapes. *ACM Transactions on Graphics (TOG)* 31(4):1–11
- Papamakarios G, Nalisnick E, Rezende DJ, Mohamed S, Lakshminarayanan B (2019) Normalizing flows for probabilistic modeling and inference. arXiv preprint arXiv:1912.02762
- Paszke A, Gross S, Massa F, Lerer A, Bradbury J, Chanan G, Killeen T, Lin Z, Gimelshein N, Antiga L, Desmaison A, Kopf A, Yang E, DeVito Z, Raison M, Tejani A, Chilamkurthy S, Steiner B, Fang L, Bai J,

- Chintala S (2019) Pytorch: An imperative style, high-performance deep learning library. In: *Advances in Neural Information Processing Systems 32*, pp 8024–8035
- Patané G (2016) Star-laplacian spectral kernels and distances for geometry processing and shape analysis. In: *Computer Graphics Forum*, Wiley Online Library, vol 35, pp 599–624
- Pedregosa F, Varoquaux G, Gramfort A, Michel V, Thirion B, Grisel O, Blondel M, Prettenhofer P, Weiss R, Dubourg V, VanderPlas J, Passos A, Cournapeau D, Brucher M, Perrot M, Duchesnay E (2012) Scikit-learn: Machine learning in python. CoRR abs/1201.0490, URL <http://arxiv.org/abs/1201.0490>, 1201.0490
- Pons-Moll G, Romero J, Mahmood N, Black MJ (2015) Dyna: A model of dynamic human shape in motion. *ACM Transactions on Graphics, (Proc SIGGRAPH)* 34(4):120:1–120:14
- Poulenard A, Rakotosaona MJ, Ponty Y, Ovsjanikov M (2019) Effective rotation-invariant point cnn with spherical harmonics kernels. arXiv preprint arXiv:1906.11555
- Qi CR, Su H, Mo K, Guibas LJ (2017) Pointnet: Deep learning on point sets for 3d classification and segmentation. *Proc Computer Vision and Pattern Recognition (CVPR)*, IEEE 1(2):4
- Remelli E, Han S, Honari S, Fua P, Wang R (2020) Lightweight multi-view 3d pose estimation through camera-disentangled representation. In: *Proceedings of the IEEE/CVF Conference on Computer Vision and Pattern Recognition*, pp 6040–6049
- Reuter M (2010) Hierarchical shape segmentation and registration via topological features of laplace-beltrami eigenfunctions. *International Journal of Computer Vision* 89(2-3):287–308
- Reuter M, Wolter FE, Peinecke N (2006) Laplace-beltrami spectra as shape-dna of surfaces and solids. *Computer-Aided Design* 38(4):342–366
- Roberts RA, dos Anjos RK, Maejima A, Anjyo K (2020) Deformation transfer survey. *Computers & Graphics*
- Rodolà E, Cosmo L, Bronstein MM, Torsello A, Cremers D (2017) Partial functional correspondence. In: *Computer Graphics Forum*, Wiley Online Library, vol 36, pp 222–236
- Rustamov RM (2007) Laplace-beltrami eigenfunctions for deformation invariant shape representation. In: *Proceedings of the fifth Eurographics symposium on Geometry processing*, Eurographics Association, pp 225–233
- Sanghi A (2020) Info3d: Representation learning on 3d objects using mutual information maximization and contrastive learning. arXiv preprint arXiv:2006.02598
- Sanghi A, Danielyan A (2019) Towards 3d rotation invariant embeddings. *CVPR 2019 Workshop on 3D Scene Understanding for Vision, Graphics, and Robotics*
- Sharp N, Crane K (2020) A laplacian for nonmanifold triangle meshes. In: *Computer Graphics Forum*, Wiley Online Library, vol 39, pp 69–80
- Shoemake K (1985) Animating rotation with quaternion curves. In: *Proceedings of the 12th annual conference on Computer graphics and interactive techniques*, pp 245–254
- Stein F, Medioni G, et al. (1992) Structural indexing: Efficient 3-d object recognition. *IEEE Transactions on Pattern Analysis and Machine Intelligence* 14(2):125–145
- Sumner RW, Popović J (2004) Deformation transfer for triangle meshes. *ACM Transactions on graphics (TOG)* 23(3):399–405
- Sun J, Ovsjanikov M, Guibas L (2009) A concise and provably informative multi-scale signature based on heat diffusion. In: *Computer graphics forum*, Wiley Online Library, vol 28, pp 1383–1392
- Sun X, Lian Z, Xiao J (2019) Srinet: Learning strictly rotation-invariant representations for point cloud classification and segmentation. In: *Proceedings of the 27th ACM International Conference on Multimedia*, pp 980–988
- Taubin G (1995) A signal processing approach to fair surface design. In: *Proceedings of the 22nd annual conference on Computer graphics and interactive techniques*, pp 351–358
- Tombari F, Salti S, Di Stefano L (2010) Unique signatures of histograms for local surface description. In: *European conference on computer vision*, Springer, pp 356–369
- Vallet B, Lévy B (2008) Spectral geometry processing with manifold harmonics. In: *Computer Graphics Forum*, Wiley Online Library, vol 27, pp 251–260
- Varol G, Romero J, Martin X, Mahmood N, Black MJ, Laptev I, Schmid C (2017) Learning from synthetic humans. In: *CVPR*
- Vinh NX, Epps J, Bailey J (2010) Information theoretic measures for clusterings comparison: Variants, properties, normalization and correction for chance. *The Journal of Machine Learning Research* 11:2837–2854
- Wang Y, Ben-Chen M, Polterovich I, Solomon J (2017) Steklov spectral geometry for extrinsic shape analysis. arXiv preprint arXiv:1707.07070
- Watanabe S (1960) Information theoretical analysis of multivariate correlation. *IBM Journal of research and development* 4(1):66–82
- Weyl H (1911) Über die asymptotische verteilung der eigenwerte. *Nachrichten von der Gesellschaft*

- der Wissenschaften zu Göttingen, Mathematisch-Physikalische Klasse 1911:110–117
- Worrall D, Brostow G (2018) Cubenet: Equivariance to 3d rotation and translation. In: Proceedings of the European Conference on Computer Vision (ECCV), pp 567–584
- Worrall DE, Garbin SJ, Turmukhambetov D, Brostow GJ (2017) Interpretable transformations with encoder-decoder networks. In: Proceedings of the IEEE International Conference on Computer Vision, pp 5726–5735
- Xiao Z, Lin H, Li R, Geng L, Chao H, Ding S (2020) Endowing deep 3d models with rotation invariance based on principal component analysis. In: 2020 IEEE International Conference on Multimedia and Expo (ICME), IEEE, pp 1–6
- Ye Z, Diamanti O, Tang C, Guibas L, Hoffmann T (2018) A unified discrete framework for intrinsic and extrinsic dirac operators for geometry processing. In: Computer Graphics Forum, Wiley Online Library, vol 37, pp 93–106
- Yin M, Li G, Lu H, Ouyang Y, Zhang Z, Xian C (2015) Spectral pose transfer. *Computer Aided Geometric Design* 35:82–94
- You Y, Lou Y, Liu Q, Tai YW, Ma L, Lu C, Wang W (2018) Pointwise rotation-invariant network with adaptive sampling and 3d spherical voxel convolution. arXiv preprint arXiv:181109361
- Zhang Z, Hua BS, Rosen DW, Yeung SK (2019) Rotation invariant convolutions for 3d point clouds deep learning. In: International Conference on 3D Vision (3DV)
- Zhou K, Bhatnagar BL, Pons-Moll G (2020) Unsupervised shape and pose disentanglement for 3d meshes. In: European Conference on Computer Vision, Springer, pp 341–357
- Zuffi S, Kanazawa A, Jacobs D, Black MJ (2017) 3D menagerie: Modeling the 3D shape and pose of animals. In: IEEE Conf. on Computer Vision and Pattern Recognition (CVPR)

A Invariant FTL-based Mapping

As an aside, in an FTL-based model, we remark that it is possible to transform $x \in \mathcal{X}$, in a way that is invariant to latent-space rotation operators. Let $\mathcal{I}[x] = (U[x]_i^T U[x]_j)_{i,j \in [1, N_s]; i \leq j}$ be the collection of inner products of the subvectors of x . Then $\mathcal{I}[x]$ is rotation invariant; i.e., $\mathcal{I}[x] = \mathcal{I}[F(R, x)]$, for any $R \in SO(3)$. This idea is noted by Worrall et al. (2017).

However, we found that using $\mathcal{I}[x]$ only slightly improved rotation invariance, yet slightly decreased reconstruction performance, and further was computationally expensive, due to the quadratic dependence of $\dim(\mathcal{I}[x])$ on N_s . Nevertheless,

this may be specific to our particular architectural setup, and could still be an interesting direction for future work.

B Evaluation Metric Details

B.1 Latent Rotation Invariance Measure

We provide a more detailed description of the latent clustering metric \mathcal{C}_X here. Recall that our goal is to take a set of random shapes (potentially differing in intrinsics, non-rigid extrinsics, and orientation) and duplicate each shape, before randomly rotating the copies. We then encode each shape into x_c -space and cluster them. We use K-means clustering (MacQueen et al., 1967) to obtain the labeling. We expect our canonicalization method to bring the latent representations close in latent space, such that rotated copies should cluster together. We can therefore measure rotational invariance by supervised clustering quality metrics, in which the instance identity (i.e., which shape a vector originated from) is a ground truth cluster label. We use Adjusted Mutual Information (AMI) for this (Vinh et al., 2010), which returns 1 for a perfect partitioning (as compared to the ground truth) and a 0 for a random clustering.

While this captures the representational invariance to rotation in the embedding space, the number of disparate sample shapes to use is unclear. We therefore average over a sequentially larger set of samples, thus giving an “area-under-the-curve”-like measure of quality across sample sizes.

More formally, let $\Gamma = \{P_1, \dots, P_{N_I}\}$ be a set of $|\Gamma| = N_I$ PC shape instances. Now consider a set that includes N_{rc} rotated copies of each PC: $\tilde{\Gamma} = \bigcup_{k=1}^{N_I} \{\tilde{P}_{k,1}, \dots, \tilde{P}_{k,N_{rc}}\}$, where $\tilde{P}_{k,j} = P_k \tilde{R}_j$ for a randomly sampled \tilde{R}_j and $|\tilde{\Gamma}| = N_I N_{rc}$. We then encode the set into canonical representations $\tilde{\Gamma}_E = \{E_x(\tilde{P}_{k,j}) \forall \tilde{P}_{k,j} \in \tilde{\Gamma}\}$ and run our clustering algorithm on $\tilde{\Gamma}_E$ to get $\text{AMI}(N_I)$ for a given instance set size N_I . Let \mathcal{N}_S be a set of sample sizes (we chose eight sizes, linearly spaced from 20 to 10^3). Finally, the x_c -space rotational consistency metric is given by

$$\mathcal{C}_X = \frac{1}{|\mathcal{N}_S|} \sum_{N_I \in \mathcal{N}_S} \text{AMI}(N_I). \quad (19)$$

Note that for each size we always run two clusterings with different randomly chosen sample shapes, and use their average AMI in the above equation. For implementations, we use scikit-learn (Pedregosa et al., 2012).

C Dataset Details

Except for HA, all our datasets are identical to those in (Aumentado-Armstrong et al., 2019). We denote N_p as the size of the input point cloud (PC) and N_λ as the dimensionality of the spectrum used. In all cases, we output the same number of points as we input.

We also perform a scalar rescaling of the dataset such that the largest bounding box length is scaled down to unit length. This scale is the same across PCs in a given dataset (otherwise the change in scale would affect the spectrum for each shape differently). For augmentation and rigid orientation learning, we apply random rotations about the gravity axis (SMAL and SMPL) or the out-of-image axis (MNIST). For rotation supervision, the orientation of the raw data is treated as canonical.

C.1 MNIST

Meshes are extracted from the greyscale MNIST images, followed by area-weighted point cloud (PC) sampling. See (Aumentado-Armstrong et al., 2019) for extraction details. We set $N_p = 512$ and $N_\lambda = 20$. The dataset has 59483 training examples and 9914 testing examples.

C.2 SMAL

Using the SMAL model (Zuffi et al., 2017), we generate set of 3D animal shapes with varying shape and pose. Using densities provided by authors, we generate 3200 shapes per animal category. Following 3D-CODED (Groueix et al., 2018), we sample poses by taking a Gaussian about the joint angles with a standard deviation of 0.2. We use 15000 shapes for training and 1000 for testing, and set $N_p = 1600$ and $N_\lambda = 24$.

C.3 SMPL

Based on the SMPL model (Loper et al., 2015), we again follow the procedure in 3D-CODED (Groueix et al., 2018) to assemble a dataset of human models. This results in 20500 meshes per gender, using random samples from the SURREAL dataset (Varol et al., 2017), plus an additional 3100 meshes of “bent” people per gender, following Groueix et al. (2018). Ultimately, we get 45992 training and 1199 testing meshes, equally divided by gender, after spectral calculations. We used $N_p = 1600$ and $N_\lambda = 20$.

C.4 Human-Animal (HA)

Since our model uses only geometry, we are able to simply mix SMAL and SMPL data together. The testing sets are left alone, and used separately during evaluation (for comparison to the unmixed models). For training, we use the entire SMAL training set, plus 9000 unbent and 1500 bent samples from the SMPL training set, per gender. We set $N_p = 1600$ and $N_\lambda = 22$.

Note that the use of a single scalar scaling factor (setting the maximum bounding box length to 1) means that SMPL models are smaller in the HA data than in the isolated SMPL dataset. We correct for this in the evaluation tables so that they are comparable (e.g., for Chamfer distances).

D Implementation Details

All models were implemented in Pytorch (Paszke et al., 2019). Notationally, let $n = \dim(x_c)$, $n_E = \dim(z_E)$, $n_I = \dim(z_I)$, and $n_R = \dim(z_R)$. For this section, we assume that the number of points N_p in a point cloud (PC) is the same for inputs and outputs (though the architectures themselves do not require this). Validation sets of size 40 (or 250 for MNIST) were set aside from the training set to observe generalization error estimates. Hyper-parameters were largely set based on qualitative examination of training outputs.

D.1 Autoencoder Details

D.1.1 AE Network Architectures

Both the STD and FTL architectures used the same network components, with slight hyper-parameter alterations. Our encoders $E_r : \mathbb{R}^{3N_p} \rightarrow \mathbb{R}^4$ and $E_x : \mathbb{R}^{3N_p} \rightarrow \mathbb{R}^n$ were implemented as PointNets (Qi et al., 2017) without spatial transformers, with hidden channel sizes (64, 128, 256, 512, 128) and (128, 256, 512, 836, 1024). The inputs are only the point coordinates (i.e., three channels) and the output is a four-dimensional quaternion for E_r and an n -dimensional vector for E_x . The decoder $D : \mathbb{R}^n \rightarrow \mathbb{R}^{3N_p}$ is implemented as a fully connected network, with hidden layer sizes (K, 2K, 4K), where $K = 1200$ for STD and $K = 1250$ for FTL. Within D , each layer consisted of a linear layer, layer normalization (Ba et al., 2016), and ReLU (except for the last, which had only a linear layer). For the MNIST dataset only, we changed the hidden layer sizes of the decoder D to be (512, 1024, 1536).

D.1.2 AE Hyper-Parameters and Loss Weights

For architectural parameters, in the FTL case, we set $N_s = 333$, and hence $n = 999$. For STD, we let $n = 600$ and did not notice improvements when increasing it. For MNIST, we set $N_s = 32$ and, for the STD case, $n = 150$. Regarding loss parameters, we set the reconstruction loss weights to $\alpha_C = 200$, $\alpha_H = 1$, $\tilde{\gamma}_P = 100$, and $\gamma_P = 20$, in the FTL case, altering only $\gamma_P = 250$ in the STD case. Rotational consistency and prediction loss weights were set to $\gamma_c = 1$ and $\gamma_r = 10$. Regularization loss weights were $\gamma_w = \gamma_d = 2 \times 10^{-5}$. For MNIST, we altered $\gamma_c = 50$ for STD, while we let $\gamma_d = 10^{-6}$, $\gamma_w = 5 \times 10^{-5}$, and $\gamma_c = 100$ for FTL.

D.1.3 AE Training Details

We train all AEs with Adam (Kingma and Ba, 2014), using an initial learning rate of 0.0005. For supervised AEs, we pretrain the rotation predictor for 2000 iterations before the rest of the network. We use a scheduler that decreases the learning rate by 5% upon hitting a loss plateau, until it reaches 0.0001. We trained MNIST, SMAL, SMPL, and HA for 200, 1250, 350, and 400 epochs, respectively, and batch sizes of 64/100 (FTL/STD) and 36/40 for MNIST and non-MNIST datasets. We set the number of rotated copies (which expands the batch sizes above) was set to $n_R = 3$, except in the case of MNIST (for which we used $n_R = 6$ in the FTL case and $n_R = 4$ in the STD case). Finally, note that, during training, for the supervised case only, we replace the predicted rotation \hat{R} with the real one R in all operations.

D.2 Variational Autoencoder Details

For implementation of the HFVAE, we use ProbTorch (Narayanaswamy et al., 2017). Our normalizing flow subnetwork used nflows (Durkan et al., 2020).

D.2.1 VAE Network Architectures

For the VAE, all networks except for the flow mapping f_λ are implemented as fully connected networks (linear-layer+norm+ReLU, as above). Approximate variational posteriors have

Table 4 VAE hyper-parameters across datasets. These values are for the GDVAE++ training method. See text in Appendix Sec. D.2.2 for details.

	β_2	β_4	ω_R	ω_Σ	ω_I	ω_λ	n_E	n_I
MNIST	50	100	350	80	600	0	4	24
SMAL	10	50	400	40	300	200	8	24
SMPL	20	100	350	80	600	0	12	20
HA	20	80	360	60	450	100	10	22

diagonal covariances. Thus, we have the following mappings with their hidden sizes:

- The rotation distribution parameter encoders, $\mu_R : \mathbb{R}^4 \rightarrow \mathbb{R}^{n_R}$ and $\Sigma_R : \mathbb{R}^4 \rightarrow \mathbb{R}^{n_R}$, are implemented with an initial shared network, with hidden sizes (256, 128) into an intermediate dimensionality of 64, followed by single linear layer each.
- The quaternion decoder $D_q : \mathbb{R}^{n_R} \rightarrow \mathbb{R}^4$ is structured as (64, 128, 256).
- The intrinsic and extrinsic parameter encoders, $\mu_\xi : \mathbb{R}^n \rightarrow \mathbb{R}^{n_\xi}$ and $\Sigma_\xi : \mathbb{R}^n \rightarrow \mathbb{R}^{n_\xi}$, for $\xi \in \{E, I\}$, have identical network architectures across latent group types: (2000, 1600, 1200, 400) and (2000, 1200, 400), for μ_ξ and Σ_ξ , respectively.
- The only mapping that is not a fully connected network is the bijective flow f_λ (and its inverse, g_λ). Recall that we use f_λ as $\tilde{\mu}$. Hence, $f_\lambda : \mathbb{R}^{N_\lambda} \rightarrow \mathbb{R}^{n_I}$ and $N_\lambda = n_I$. This is implemented as a normalizing flow with nine layers, where each layer consists of an affine coupling transform (Dinh et al., 2016), an activation normalization (actnorm) (Kingma and Dhariwal, 2018), and a random feature ordering permutation. The last layer does not have normalization or permutation. Each affine coupling uses an internal FC network with one hidden layer of size 400.
- For the GDVAE++ training regime, we require a covariance parameter estimator for inference during training: $\Sigma_\xi : \mathbb{R}^{N_\lambda} \rightarrow \mathbb{R}^{n_I}$. This is implemented via hidden layers (2n_I, 2n_I).
- The shape decoder $D_x : \mathbb{R}^{n_I+n_E} \rightarrow \mathbb{R}^n$ is an FC network with hidden layers 600, 1200, 1600, 2000.

D.2.2 VAE Hyper-Parameters and Loss Weights

Recall that the loss hyper-parameters control the following terms: the intra-group total correlation (TC) β_1 , dimension-wise KL divergence β_2 , mutual information β_3 , inter-group TC β_4 , log-likelihood reconstruction ω_R , relative quaternion reconstruction ω_q , flow likelihood ω_p , intrinsics consistency in z_I -space ω_I , intrinsics consistency in λ -space ω_λ , covariance disentanglement ω_Σ , and Jacobian disentanglement $\omega_\mathcal{J}$.

In all cases, we set $n_R = 3$, $\beta_1 = 1$, $\beta_3 = 1$, $\omega_p = 1$, $\omega_\mathcal{J} = 200$, and $\omega_q = 10$. See Table 4 for dataset-dependent parameters. An additional L_2 weight decay was applied to all networks, with a strength of 10^{-4} . For the flow-only (GDVAE-FO) approach, the parameters are the same per dataset, except for ω_I and ω_λ (which were tuned more in line with original GDVAE model, in an effort to improve disentanglement). For the FO case, we set $\omega_\lambda = 800$ and ω_I to 0, 250, and 0, for SMAL, SMPL and HA, respectively.

D.2.3 VAE Training Details

As in the AE case, optimization is done with Adam, using a reduce-on-plateau scheduler. The initial learning rate was

set to 0.0001, with a minimum of 0.00001. A batch size of 264 was used, except for MNIST, for which we used 512. The networks were trained for 25000 iterations for MNIST and 40000 iterations for all other datasets. We note that for the GDVAE++ mode only, we also cut the gradient of the ω_I loss term from flowing through $\tilde{\mu}_I$ (preventing extrinsic information in μ_I from contaminating $\tilde{\mu}_I$).